

ARMY RESEARCH LABORATORY



Slip Continuity in Explicit Crystal Plasticity Simulations Using Nonlocal Continuum and Semi-discrete Approaches

by Richard Becker

ARL-TR-6307

January 2013

NOTICES

Disclaimers

The findings in this report are not to be construed as an official Department of the Army position unless so designated by other authorized documents.

Citation of manufacturer's or trade names does not constitute an official endorsement or approval of the use thereof.

Destroy this report when it is no longer needed. Do not return it to the originator.

Army Research Laboratory

Aberdeen Proving Ground, MD 21005

ARL-TR-6307

January 2013

Slip Continuity in Explicit Crystal Plasticity Simulations Using Nonlocal Continuum and Semi-discrete Approaches

Richard Becker
Weapons and Materials Research Directorate, ARL

REPORT DOCUMENTATION PAGE				<i>Form Approved OMB No. 0704-0188</i>
<p>Public reporting burden for this collection of information is estimated to average 1 hour per response, including the time for reviewing instructions, searching existing data sources, gathering and maintaining the data needed, and completing and reviewing the collection information. Send comments regarding this burden estimate or any other aspect of this collection of information, including suggestions for reducing the burden, to Department of Defense, Washington Headquarters Services, Directorate for Information Operations and Reports (0704-0188), 1215 Jefferson Davis Highway, Suite 1204, Arlington, VA 22202-4302. Respondents should be aware that notwithstanding any other provision of law, no person shall be subject to any penalty for failing to comply with a collection of information if it does not display a currently valid OMB control number.</p> <p>PLEASE DO NOT RETURN YOUR FORM TO THE ABOVE ADDRESS.</p>				
1. REPORT DATE (DD-MM-YYYY) January 2013	2. REPORT TYPE		3. DATES COVERED (From - To) October 2010 to September 2012	
4. TITLE AND SUBTITLE Slip Continuity in Explicit Crystal Plasticity Simulations Using Nonlocal Continuum and Semi-discrete Approaches			5a. CONTRACT NUMBER	
			5b. GRANT NUMBER	
			5c. PROGRAM ELEMENT NUMBER	
6. AUTHOR(S) Richard Becker			5d. PROJECT NUMBER FY11-WMR-017	
			5e. TASK NUMBER	
			5f. WORK UNIT NUMBER	
7. PERFORMING ORGANIZATION NAME(S) AND ADDRESS(ES) U.S. Army Research Laboratory ATTN: RDRL-WMP-C Aberdeen Proving Ground, MD 21005			8. PERFORMING ORGANIZATION REPORT NUMBER ARL-TR-6307	
9. SPONSORING/MONITORING AGENCY NAME(S) AND ADDRESS(ES)			10. SPONSOR/MONITOR'S ACRONYM(S)	
			11. SPONSOR/MONITOR'S REPORT NUMBER(S)	
12. DISTRIBUTION/AVAILABILITY STATEMENT Approved for public release; distribution unlimited.				
13. SUPPLEMENTARY NOTES				
14. ABSTRACT Slip continuity across element boundaries in explicit finite element simulations is enforced through nonlocal penalty constraints applied to continuum crystal plasticity relations and in a nonlocal, semi-discrete crystal slip model. The continuity constraints provide additional coupling within the plastic deformation field, and a length scale effect is introduced. The deformation field becomes more diffuse with reduced physical size of the model region and the strength increases. The semi-discrete method produces dislocation pile-ups and slip gradients along discrete slip planes, but the simulation approach is ultimately unsatisfactory. Consideration of the physical spacing of dislocations and the typical size of dislocation cells in deformed metals elicits concerns about the applicability of continuum slip models with sub-micron spatial resolution.				
15. SUBJECT TERMS Crystal plasticity, nonlocal, gradient, dislocation				
16. SECURITY CLASSIFICATION OF:		17. LIMITATION OF ABSTRACT UU	18. NUMBER OF PAGES 48	19a. NAME OF RESPONSIBLE PERSON Richard Becker
a. REPORT Unclassified	b. ABSTRACT Unclassified			c. THIS PAGE Unclassified

Contents

List of Figures	v
List of Tables	vi
Acknowledgment	vii
1. Introduction	1
2. Continuum Model for Slip Continuity	2
2.1 Crystal Kinematics	3
2.2 Nonlocal Model.....	3
2.3 Crystal Flow Strength.....	5
2.4 Crystal Geometry and Boundary Conditions	6
2.5 Finite Element Implementation	6
3. Continuum Finite Element Results	7
3.1 Single Crystal	7
3.1.1 Nonlocal Strength.....	7
3.1.2 Stress State	9
3.1.3 Slip Rate	9
3.1.4 Stress Strain Response.....	10
3.1.5 Mesh Refinement	11
3.1.6 Time Step Instability	12
3.2 Polycrystal	13
3.2.1 Slip Rate	14
3.2.2 Nonlocal Strengthening	14
3.2.3 Polycrystal Stress-strain Behavior.....	16
4. Considerations for Discreteness of Dislocations	17
4.1 Semi-discrete Dislocation Model	18
4.2 Semi-discrete Simulation Results.....	20
4.2.1 Low Density of Nucleation Sites.....	20
4.2.2 Moderate Density of Nucleation Sites.....	25

4.2.3	Reduced Element Size.....	26
4.2.4	Stress-strain Response from Semi-discrete Model.....	28
5.	Discussion	30
6.	Conclusion	32
7.	References	34
Distribution List		37

List of Figures

Figure 1. Initial configuration for the single crystal and the crystal lattice orientation. The bottom is fixed and the top is moved to the right. Periodic boundary conditions are applied coupling the left and right hand sides.	7
Figure 2. Distribution of the nonlocal contribution to the strength on the slip system aligned vertically in the crystal, for the crystal thicknesses indicated, at shear strains of 0.03 and 0.05.....	8
Figure 3. Distribution of the normalized slip rate for single crystals of the indicated thickness and at shear strains of 0.03 and 0.05. The slip rates are normalized by the applied shear rate.....	10
Figure 4. Shear stress-shear strain response predicted for the four crystal thicknesses.	11
Figure 5. Comparison of nonlocal stress and the slip rate for the 20x100 and 40x200 element simulations of the 5- μm -thick single crystal. The results are shown at a 0.05 shear strain.....	12
Figure 6. Grain structure (a) and finite element mesh and (b) for the polycrystal simulations....	13
Figure 7. Normalized slip rate distribution for simple shear deformation of idealized polycrystals with heights of 330, 33, and 3.0 μm . The color scale is the same for all three plots.....	14
Figure 8. Nonlocal strength contributions on the three slip systems for polycrystal model sizes of 330, 33, and 3.3 μm . The color scales are consistent within each row.....	15
Figure 9. Shear stress strain response for three different size scales of idealized polycrystals..	16
Figure 10. Change in crystal lattice orientation, in degrees, at 0.025 shear strain for the 330- and 3.3- μm high polycrystals.....	17
Figure 11. Number of dislocations passing through each element for the discrete dislocation simulations of three single crystal sizes indicated. The color levels for the 5- and 10- μm crystals are the same. The center 80 μm is omitted from the 100- μm crystal to highlight the gradients at the top and bottom surfaces.....	21
Figure 12. Number of dislocations passed through each element along the 13 active slip planes in figure 11 for the 10- μm -high crystal plotted against the through thickness location. The light lines are the individual results and the heavy, dark line is the average....	22
Figure 13. Number of dislocations currently within each element for the discrete dislocation simulations of three single crystal sizes. The color levels for the 5- and 10- μm crystals are the same. The center 80 μm is omitted from the 100- μm crystal to highlight the gradients at the top and bottom surfaces.....	23
Figure 14. Plots of the in-plane stress components at a strain of 0.01 for the 10- μm -high single crystal deforming by discrete single slip on 13 slip planes.....	24
Figure 15. Number of dislocations within each element for discrete dislocation simulations of the 5- and 10- μm single crystals with a moderate density of nucleation sites.	25
Figure 16. Shear stress distribution for 10- μm -thick crystal simulation with a moderate dislocation nucleation site density	26

Figure 17. Number of dislocations currently within each element for the discrete dislocation simulations of three single crystal sizes. The color levels for the 1- and 2- μm crystals are the same. The center 16 μm is omitted from the 20- μm crystal to highlight the gradients at the top and bottom surfaces.	27
Figure 18. Shear stress distribution for the 10 $\mu\text{m} \times 2 \mu\text{m}$ crystal in a calculation with an element size of 0.025 μm and 172 dislocation nucleation sites. The stress gradients are under-resolved.....	28
Figure 19. Shear stress-strain response for the semi-discrete crystal simulations of section 4. The legends and arrows show the model width, crystal aspect ratio, element length, and the percent of elements containing dislocation nucleation sites along with the corresponding nucleation site density. Curves of the same color have the same element size and element site nucleation percentage but different model aspect ratios.....	29

List of Tables

Table 1. Average number of dislocations per element expected in the simulations of section 3.1 for well-annealed, lightly deformed, and heavily deformed metals.	18
-----------------------------------------------------------------------------------------------------------------------------------------------------------------------	----

Acknowledgment

I am grateful for the support of this work through the Director's Research Initiative at the U.S. Army Research Laboratory FY11-WMR-017.

INTENTIONALLY LEFT BLANK.

1. Introduction

Traditional metal plasticity models, formulated in terms of strain rates and stresses and incorporated in large-scale numerical analyses, provide useful solutions for a wide range of problems. Details of the material microstructure interactions that govern the deformation response are assumed to occur at length scales not resolvable by the simulations and are captured implicitly in the constitutive relations. For example, dependence of the yield strength on grain size through the Hall-Petch effect can be incorporated by including grain size in the constitutive model without tracking the details of dislocation interactions with grain boundaries.

In simulations with spatial resolution at or below the micron level, as in multiscale modeling, the length scales dictating some hardening mechanisms are correlated with gradients in the plastic strain field. The torsion experiments of Fleck et al. (1994) clearly demonstrate increased strength with decreasing size for wires 10's of microns in diameter. The size effect was further observed in bending (Stölken and Evans, 1998) and indentation (Saha, et al. 2001), and in many subsequent studies. The strengthening is attributed to gradients in the crystal lattice orientation. These gradient microstructures both store energy and provide resistance to further dislocation motion (Lee et al., 1989; Fleck and Hutchinson, 1997; Gao et al., 1999; Baskaran et al., 2010; Schouwenaars et al., 2010). Applying traditional crystal plasticity models (Asaro, 1983; Peirce et al., 1983) to investigate the size scale effect in a multiscale framework will not be successful because the models are formulated in terms of traditional continuum variables of strain rate and stress, and there is no underlying microstructure length scale that would produce a size effect.

Numerous studies over more than a decade have investigated ways to incorporate a length scale into continuum crystal plasticity models. Most focus on microstructure gradients, as it is recognized that both the Hall-Petch effect and the size scale results are tied to gradients. To cite just a few of the many examples, models have examined: continuously distributed dislocations (Acharya, 2001), dislocation density gradients (Arsenlis et al., 2004), gradient related state variables (Gurtin et al., 2007; Gerken and Dawson, 2008), and micro-polar theories (Mayeur et al., 2011). Many formulations introduce additional variables into the solution, which must be determined in concert with the standard degrees of freedom.

When using the traditional crystal plasticity model in a finite element code, the deformation of neighboring elements is only connected through shared nodal displacements and force equilibrium at the nodes. Even though dislocations associated with slip travel through the material, the transmission of dislocations from one element to another is not represented in the model, and the impact of coordinated slip on the deformation field is not captured. The indirect result is that all finite element boundaries are infinite sources and sinks for dislocations. Advanced crystal plasticity formulations, such as those based on lattice orientation gradients,

often include the continuity of dislocation flux across finite element boundaries as a byproduct because lattice orientation gradients are created by an accumulation of like-signed dislocations.

The goal of this work is to determine if a simpler approach can be used to address the length scale dependence and other deficiencies of the classical crystal plasticity model. The starting point is simply enforcing dislocation flux continuity across finite element boundaries. Different slip conservation approaches were examined by Hirschberger et al. (2011). A choice is made to implement the model in an explicit finite element code using an operator-split approach, where it is assumed that the time steps are sufficiently small that the coupled mechanics can be applied consecutively over a time step rather than concurrently. In this approach, the slip in the elements can be treated as a normal state variable, whereas it would be most effective to treat it as a degree of freedom in fully coupled, implicit solutions. The code uses existing solution variables, and the boundary conditions are conceptually straightforward. Dislocation flux is unconstrained at free surfaces, zero at rigid boundaries, and intermediate at grain boundaries that are sources and sinks for dislocations. The flux gradients can be used to infer the evolution of dislocation gradients that lead to lattice orientation gradients.

Initial work to explore the feasibility and potential impact of enforcing dislocation flux between elements in a crystal plasticity model used a special purpose, explicit dynamic code that calculated and enforced an average slip rate on element boundaries in a multi-step constitutive evaluation (Becker, 2011). The results showed the desired effects of smoothing the deformation field and increasing the hardening rate with smaller sample sizes. However, the solution technique permitted spatially oscillatory fields, particularly near the boundaries, so an alternative method for enforcing slip continuity between elements was indicated.

The report begins with an outline of the nonlocal, gradient crystal plasticity model and its implementation, and results are presented for single crystal and polycrystal simulations. Consideration of details of the microstructure at micron size scales prompted exploration and evaluation of the semi-discrete approach. The discussion expounds on concerns about the adequacy of continuum crystal plasticity models to represent microstructures at sub-micron resolution.

2. Continuum Model for Slip Continuity

The goal is to develop an enhancement to traditional continuum crystal plasticity models that can be readily incorporated into existing finite element implementations and run with minimal additional computational overhead. This objective is facilitated by targeting explicit dynamic solutions where, because of the relatively small time steps, it is often possible to impose additional constraints through an operator-split approach in which the physics are applied

sequentially within a time step rather than concurrently. In the current context, the operator split results in the constraint application lagging one time step behind its evaluation.

2.1 Crystal Kinematics

The crystal plasticity model and implementation used in the explicit dynamic finite element simulations is described in Becker (2004). It follows from the widely used kinematic framework given by Asaro (1983) with modifications to incorporate an equation of state for high pressure applications. The deformation gradient, \mathbf{F} , is notionally decomposed into elastic and plastic parts, \mathbf{F}^e and \mathbf{F}^p , respectively;

$$\mathbf{F} = \mathbf{F}^e \cdot \mathbf{F}^p. \quad (1)$$

The elastic part accounts for distortion and rotation of the crystal lattice, and the plastic part represents slip on predefined crystal planes and directions that moves material but does not alter the underlying crystal lattice.

The velocity gradient obtained from this kinematic description comprises an additive decomposition of an elastic part and an inelastic part associated slip on predefined slip systems:

$$\frac{d\dot{\mathbf{x}}}{dx} = \dot{\mathbf{F}} \cdot \mathbf{F}^{-1} = \dot{\mathbf{F}}^e \cdot \mathbf{F}^{e-1} + \sum_{\alpha=1}^{N_{sys}} \dot{\gamma}^\alpha \mathbf{s}^\alpha \otimes \mathbf{m}^\alpha. \quad (2)$$

\mathbf{s}^α and \mathbf{m}^α are, respectively, vectors of the current slip directions and slip plane normals associated with each of the slip systems (superscript α), and $\dot{\gamma}^\alpha$ are the corresponding slip rates. The slip direction and normal vectors rotate and distort with the crystal lattice as the material deforms.

2.2 Nonlocal Model

In conventional crystal plasticity analyses using an explicit dynamic finite element code with uniform strain elements, the slip rates are evaluated at each time step using the velocity gradient, the crystal strength, and any history variables associated with the element. There is no direct connection among the slip rates in neighboring elements. In order to enforce slip continuity between elements, a penalty approach is proposed. Differences in accumulated slip between adjacent elements will either increase or decrease the resistance to further slip on that slip system. This requires information from neighboring elements, making it a nonlocal method.

The basis for the model is that dislocations move along the slip direction from one element to another. The flux of dislocations crossing an element boundary for each slip system is

$$\dot{\phi} = \rho_{dis}^\alpha v^\alpha \mathbf{s}^\alpha \cdot \mathbf{n}_f, \quad (3)$$

where ρ_{dis}^α is the dislocation density, v^α is the dislocation velocity, and \mathbf{n}_f is the outward normal to the given element face. Continuity is enforced by requiring that the dislocation flux exiting

through an element face equals the flux entering the adjacent element through the common face. The dot product in equation 3 accounts for the orientation of the slip system with respect to the element face. It is zero if the slip direction is parallel to the face. This provides the opportunity for sharp jumps in slip rates across parallel slip planes while enforcing continuity along slip planes.

The dislocation density, velocity, and the Burgers vector, b , are related to the continuum slip rate by Orowan's equation

$$\dot{\gamma}^\alpha = \rho_{dis}^\alpha v^\alpha b. \quad (4)$$

For a shared element face, and assuming that the Burgers vector is constant and that the slip directions are closely aligned across the interface, the continuity error in the accumulated dislocation flux between elements can be approximated as

$$[(\gamma^\alpha)_{neighbor} - (\gamma^\alpha)_e] \mathbf{s}^\alpha \cdot \mathbf{n}_f = E_f^\alpha \quad (5)$$

The subscripts e and $neighbor$ on the accumulate slip, γ^α , denote, respectively, the element of interest and the neighbor sharing the face. The approach taken is to penalize the error. It is not necessary to assume that the Burgers vectors are equal or that the slip directions in the adjacent elements are aligned, but these simplifications are made for expedience and coding clarity in this initial implementation.

Application of equation 5 in a penalty method requires a cumulative result over all element faces. This is complicated by the changing algebraic sign of the dot product for different element faces and the 50% probability that the accumulated slips are negative. The sign of the dot product is irrelevant to the physical problem, so the absolute value is taken. The algebraic sign of the slip is also unimportant, and the magnitude is obtained by multiplying by the sign of the slip. This is preferred to using the absolute values of the slips in cases where the sign of the slip is different in the neighboring element. With these adjustments, the driving force for the penalty method, equation 5, is summed as

$$\frac{1}{\sum |\mathbf{s}^\alpha \cdot \mathbf{n}_f|} \sum_{f=1}^{N_{faces}} \frac{1}{L_f} \text{Sign}(\gamma^\alpha) [(\gamma^\alpha)_{neighbor} - (\gamma^\alpha)_e] |\mathbf{s}^\alpha \cdot \mathbf{n}_f| = E^\alpha \quad (6)$$

L_f is the distance between element centroids associated with the particular element face. It is intended to provide a larger penalty if the slip difference occurs on a smaller spatial grid. E^α in equation 6 is a weighted sum of unsigned slip gradients on a slip system for a given element. If the value is positive, slip is deficient in the element and additional slip is promoted. If the value is negative, further slip is impeded. It is significant that a constant gradient results in face contributions that sum to zero. Hence, a constant gradient is not suppressed. The excess dislocations associated with the gradient are assumed to be uniformly distributed.

A closer look at equation 6 for the special case of a slip direction aligned with a regular rectangular mesh reveals a serendipitous connection to published gradient theories. Assuming that the signs of the slips are the same and performing the summation,

$$\frac{\gamma_{e-1}^\alpha - 2\gamma_e^\alpha + \gamma_{e+1}^\alpha}{2L_f} = E^\alpha. \quad (7)$$

Subscripts $e-1$ and $e+1$ denote elements on either side of element e . Dividing equation 7 by L_f , this becomes the finite difference form for half of the second derivative of the slip along the slip direction. The second derivative appears in the micro force balance in several gradient formulations (e.g., Bittencourt et al., 2003; Gurtin et al., 2007). Hence, with a small coding change, the implementation can approximate a simplified version of an established gradient model. Because of this connection to established models, and since it gives a nonlinear length scale dependence, the modified relation

$$\frac{1}{\Sigma |\mathbf{s}^\alpha \cdot \mathbf{n}_f|} \sum_{f=1}^{N_{faces}} \frac{1}{L_f^2} \text{Sign}(\gamma^\alpha) [(\gamma^\alpha)_{neighbor} - (\gamma^\alpha)_e] |\mathbf{s}^\alpha \cdot \mathbf{n}_f| = \tilde{E}^\alpha \quad (8)$$

is used for the nonlocal simulations.

2.3 Crystal Flow Strength

The rate dependent crystal constitutive model relates the loading on each slip system to the slip rate. The driving force for slip, τ^α , is the resolved shear stress on the slip system.

$$\tau^\alpha = \mathbf{m}^\alpha \cdot \boldsymbol{\sigma} \cdot \mathbf{s}^\alpha, \quad (9)$$

where $\boldsymbol{\sigma}$ is the Cauchy stress. A simple power law rate model is used here to determine the slip rate for the applied loading.

$$\dot{\gamma}^\alpha = \dot{\gamma}_0^\alpha \left(\left| \frac{\tau^\alpha}{g^\alpha} \right| \right)^{1/m} sign(\tau^\alpha). \quad (10)$$

A low rate exponent, $m = 0.005$, is chosen to provide nearly rate-independent behavior while still smoothing the transition from elastic to plastic response at the slip system flow strength, g^α .

The flow strength is adjusted, based on the nonlocal contribution, to increase or reduce the resistance to continued deformation

$$g^\alpha = g_0^\alpha - \mu p_1 \tanh \left(b^2 \tilde{E}^\alpha \frac{p_2}{p_1} \right) \quad (11)$$

Here, p_1 and p_2 are dimensionless parameters, μ , is some average shear modulus for the crystal, and b is the Burgers vector. The base crystal strength, g_0^α , could be a function of slip to capture strain hardening, but it is assumed constant in these analyses to simplify interpretation of the results. The hyperbolic tangent function is used to cap the influence of the nonlocal term. The contribution is approximately linear, $\sim \mu p_2 b^2 \tilde{E}^\alpha$, while the argument is small, and it is capped at

a constant value of $\pm \mu p_1$. The penalty parameters are chosen as $p_1 = 5 \times 10^{-4}$ and $p_2 = 10000$. In all of the nonlocal continuum simulations: the base flow strength is $g_0^\alpha = 33.33$ MPa; the density is $\rho_0 = 2.7$ g/cm³; the Burgers vector is $b = 0.3$ nm; and shear modulus is $\mu = 25,650$ MPa.

2.4 Crystal Geometry and Boundary Conditions

An idealized two-dimensional crystal geometry is used for these analyses. The crystal consists of three slip systems set in an equilateral triangle configuration. This allows a multitude of slip modes, but redundant slip is unlikely. In the rate independent limit, it is not possible to have slip on all three systems simultaneously, and the rate sensitivity is too low to enable redundant slip activation in these simulations.

Constant strain quadrilateral elements with hourglass control (Flanagan and Belytschko, 1981) are used for all of the simulations. Elements in which all four faces are adjacent to an element of the same initial orientation are interior elements, and gradients are computed directly as indicated in equation 8. Elements with fewer than four faces contacting regions of the same orientation are either on grain boundaries or model boundaries. The face is flagged for these elements, and a parameter is checked to see whether it is treated as a zero flux boundary or a free boundary with no slip impedance. For the non-interior elements with zero-flux boundaries, ghost elements with opposite slip are assumed across the flagged faces. Grain boundaries and surfaces with applied boundary conditions are treated in this manner. For free surfaces and periodic boundaries, the ghost element across the flagged face is set with the same slip so that these interfaces do not contribute to the gradient.

2.5 Finite Element Implementation

The model was implemented in the large-scale parallel, explicit finite element code ALE3D (2012). The crystal plasticity constitutive model existed previously (Becker, 2004) and the strengthening terms in equation 11 due to the nonlocal effects were a straightforward addition.

The nonlocal computations occur outside of the material model when all history variables are at a consistent state. Since it is an Arbitrary Lagrange-Eulerian code that moves material through the mesh, many features and functions are already in place for the nonlocal calculations. Lists of neighboring elements and shared faces exist, as do functions accessing history variables in the adjacent elements. For parallel computations, the problem is subdivided into domains that reside on separate processors. Elements that are at the boundaries of these domains have neighboring elements that reside on other processors. The information from the neighboring elements residing on other processors is carried locally in ghost elements, so all of the data needed to perform the nonlocal calculations of equation 8 are available locally on each processor. A communication call prior to the nonlocal calculations assures that all of the information is current. A significant amount of bookkeeping and data juggling is required, but the computations in equation 8 are straightforward.

3. Continuum Finite Element Results

The effect of the slip continuity constraint (slip gradient) is evaluated on two configurations, each at multiple length scales. All simulations are two-dimensional. The first configuration is simple shear of a single crystal with one of the slip planes initially aligned orthogonal to the shear direction. This creates single slip conditions for a straightforward evaluation of the model. The second configuration is a polycrystal constructed from regular hexagons. The orientation of the crystal lattice for each grain is random.

3.1 Single Crystal

Single crystal calculations were run at four size scales using a 20×100 mesh of square elements (figure 1). Velocity boundary conditions are applied to the upper and lower surfaces to shear the top of the crystal to the right. Initial velocities of all interior nodes are prescribed consistent with simple shear to eliminate ringing as the explicit dynamic calculation starts. Periodic boundary conditions are applied to the lateral surfaces to mimic an infinitely wide crystal. The heights of the single crystals simulated were 50, 5, 1, and $0.5 \mu\text{m}$, and the width of the simulation box was 20% of the height in each case. Although the width is irrelevant with the periodic boundary conditions, multiple elements are used across the width to demonstrate that the boundary conditions are applied properly. Slip transmission is restrained on the upper and lower boundaries, and slip transmission is unimpeded on the lateral, periodic boundaries.

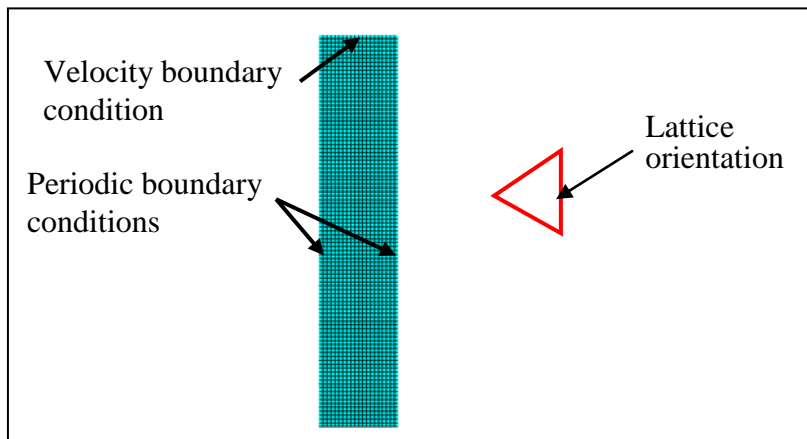


Figure 1. Initial configuration for the single crystal and the crystal lattice orientation.
The bottom is fixed and the top is moved to the right. Periodic boundary conditions are applied coupling the left and right hand sides.

3.1.1 Nonlocal Strength

The nonlocal strength contribution to equation 11 is shown in figure 2 for the four crystal sizes and at two shear strains. The largest crystal is on the left and the smallest is on the right. The top row shows the distribution at a shear strain of 0.03 and bottom shows the results at an average

shear strain of 0.05. The color scales are different for each crystal size, but the scales at each crystal size are the same at 0.03 and 0.05 shear strains to highlight the evolution.

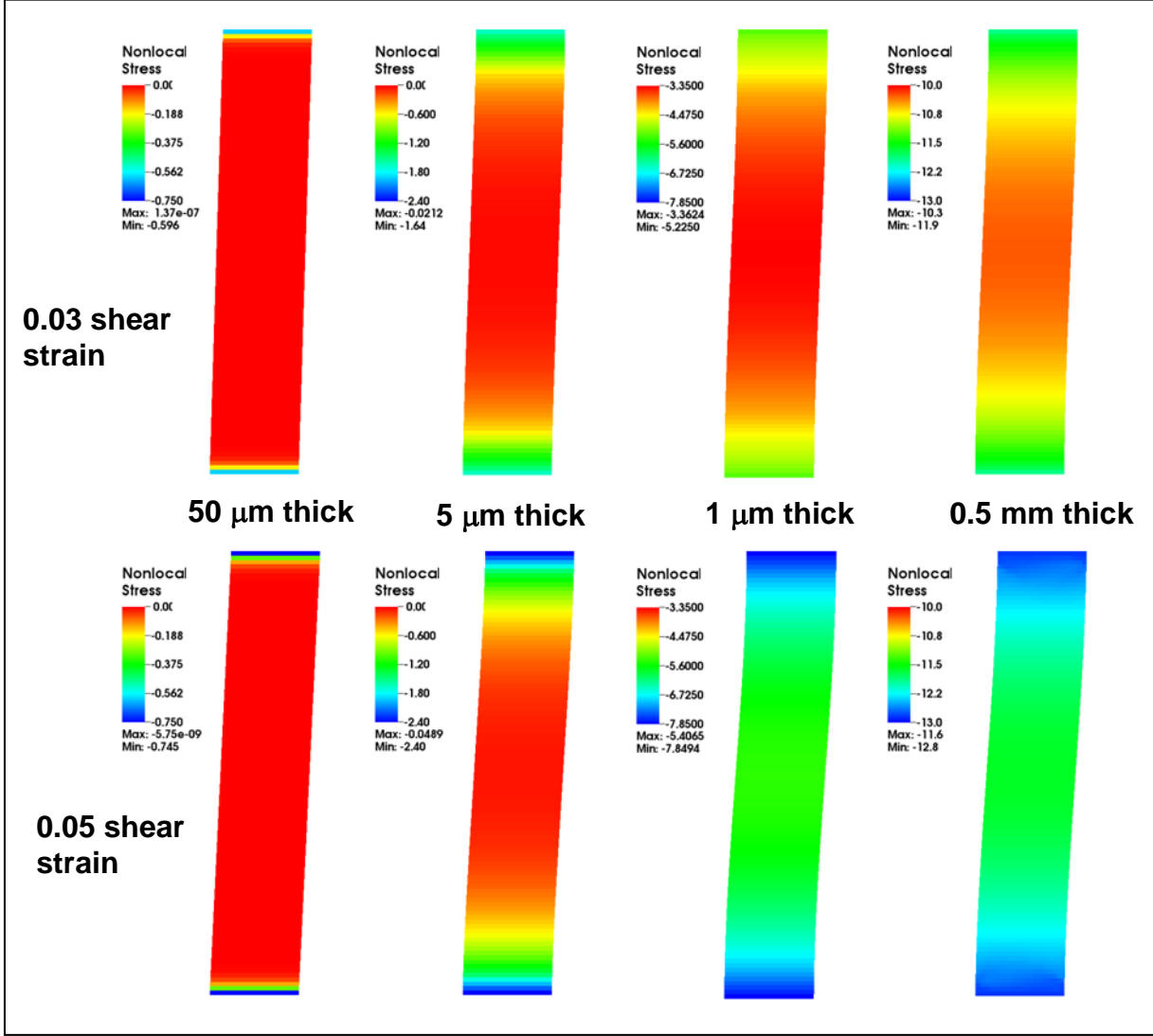


Figure 2. Distribution of the nonlocal contribution to the strength on the slip system aligned vertically in the crystal, for the crystal thicknesses indicated, at shear strains of 0.03 and 0.05.

The magnitude of the nonlocal strength contribution and the relative depth that the distribution penetrates from the surfaces increases as the crystal thickness is decreased. The sharpest gradients are expected at the crystal surfaces where the slip transmission is impeded. For the 50- μm crystal the strength is increased only within a few elements of the surface, corresponding to a few microns. The central portion of the crystal sees no gradient or strengthening effect, even as the strain increases from 0.03 to 0.05. The boundary layer also appears to penetrate a few microns in the 5- μm -thick crystal simulation. However, a smaller portion of the crystal is nearly free of gradient effects for this smaller crystal. At yet smaller crystal thicknesses, the gradient effect penetrates the full crystal thickness, and the evolution with increasing deformation is

evident. The strength at the center is elevated significantly by a strain of 0.03, and it continues to increase with further deformation.

The minimum and maximum values are indicated in each of the plots. Except for the smallest crystal, the difference between the maximum and minimum increases as the crystal size decreases and the difference also increases with increasing strain. The increase with strain indicates that the gradient is still evolving at a shear strain of 0.05. The trends are different for the 0.5- μm crystal because the gradient strengthening is beginning to run up against the cap set by the hyperbolic tangent function in equation 11. With continued deformation, the gradient strengthening is becoming more uniform, albeit at a higher level.

3.1.2 Stress State

The momentum balance in the vertical direction (y -direction) dictates that the y -gradient in the y -direction stress component is balanced by the horizontal (x -direction) gradient in the shear stress. Since the periodic boundary conditions require that all horizontal gradients are zero, the stress in the y -direction should be constant. The magnitude of the y -direction stress is not determined by the momentum equation, just that it is constant. The calculations show a constant y -direction stress to five significant digits.

More important for current purposes is the momentum balance in the horizontal direction. The lack of stress gradients in the horizontal direction requires the shear stress to be constant through the thickness. The simulations show that the shear stress is constant to five significant digits. While the x -direction stress must be constant in the x -direction, the symmetry conditions and momentum equations provide no further constraints restricting its gradient in the y -direction.

3.1.3 Slip Rate

The normalized slip rates corresponding to the configurations in figure 2 are shown in figure 3. Again, the largest crystal is on the left and the smallest is on the right. The top row contains results at a shear strain of 0.03, and bottom row shows the normalized slip rate at a shear strain of 0.05. The plots are normalized by the applied shear strain rate so that a value of 1.0 would indicate a uniform shear. Since the shear stress and the reference strength in equation 11 are both constant, the slip rate is approximately related to the gradient term through equations 10 and 11. Second-order factors influencing the slip rate include the change in lattice orientation and non-zero components of the x -direction and y -direction stresses that modify the resolved shear stress.

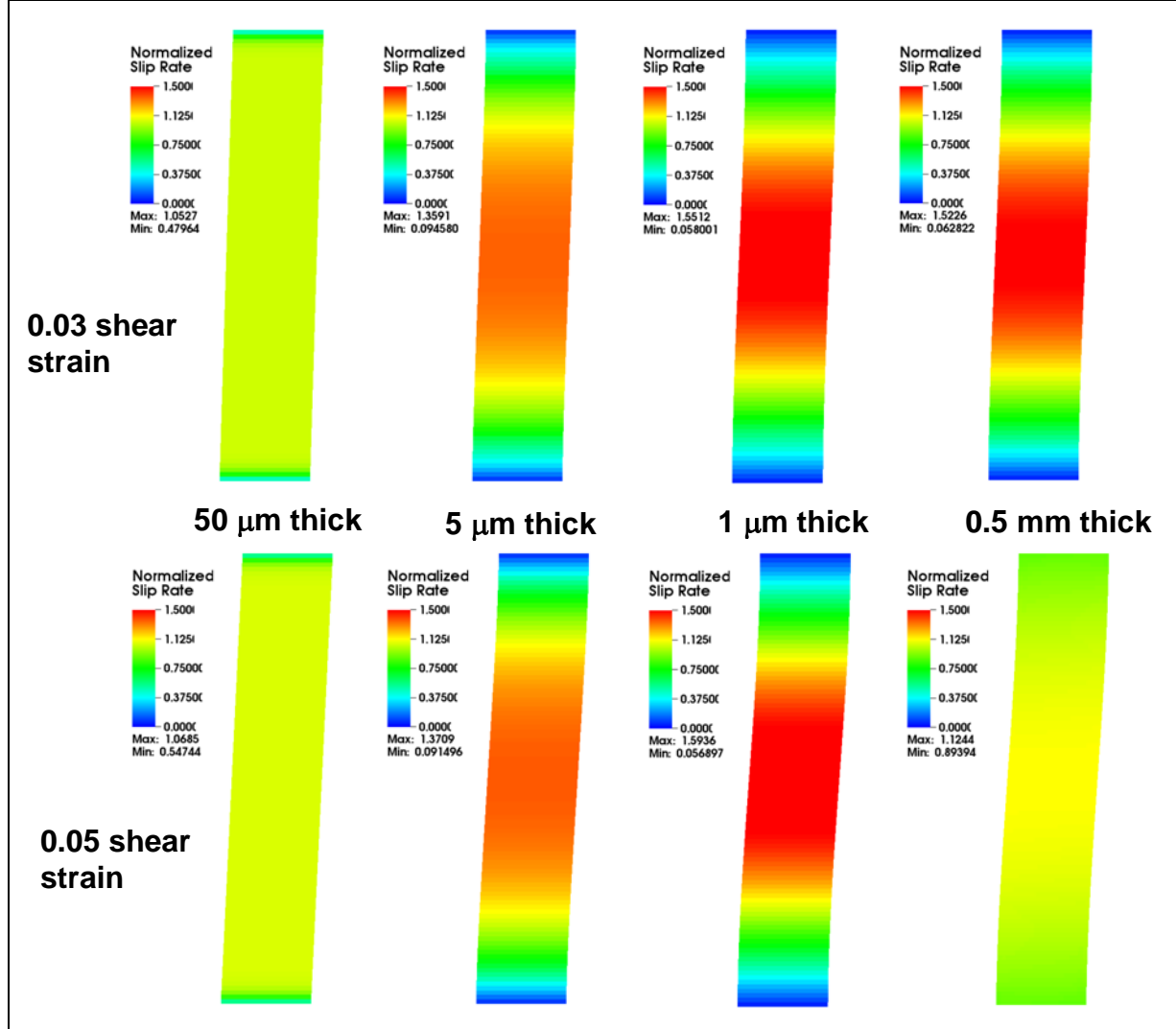


Figure 3. Distribution of the normalized slip rate for single crystals of the indicated thickness and at shear strains of 0.03 and 0.05. The slip rates are normalized by the applied shear rate.

The slip rate follows the same trends as the nonlocal hardening contribution. The variation in slip rate is greater for the smaller crystals; and, except for the smallest crystal, the differences are greater with increased deformation. As a result of the boundary conditions, slip rates are low at top and bottom boundaries compared to the center regions. This results in the sigmoidal deformed shapes. More severe differences in slip rate result in greater deviation from a linear shear deformation profile. The slip rates for the 0.5-μm crystal become more uniform at the higher deformation because the gradient term is capped by the hyperbolic tangent function. The strength is more uniform, which results in a more uniform slip rate.

3.1.4 Stress Strain Response

The shear stress-shear strain responses for the various crystal thicknesses are plotted in figure 4. The curves are identical through the linear elastic regime, and all yield at approximately the same

stress, approximately 34 MPa. The applied shear rate is 50 times the reference shear rate; and, accounting for the strain rate sensitivity, the apparent yield strength is calculated from equation 10 to be 33.99 MPa rather than the reference shear strength of 33.33 MPa.

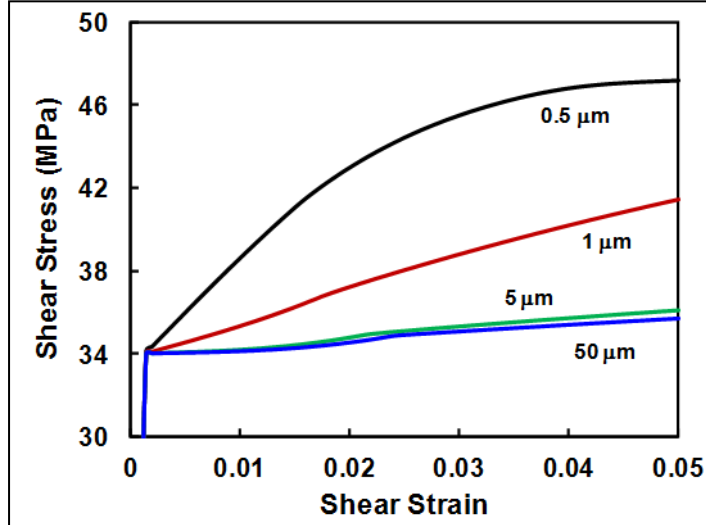


Figure 4. Shear stress-shear strain response predicted for the four crystal thicknesses.

The stress shows the expected trend of increasing strength at the smaller crystal sizes. This is directly related to the nonlocal strength in figure 2. The nonlinear dependence on specimen dimensions is due to dividing by the element size squared in equation 8. The strain hardening rate is fairly consistent with increasing strain for the three larger crystal sizes but not for the smallest. Stress in the 0.5-μm crystal peaks as the hyperbolic tangent function places a cap on the nonlocal strength contribution. This is also consistent with the results presented in figures 2 and 3. A final observation from figure 4 is the kink that is most evident in the larger two specimens near a strain of 0.02. This marks the transition from single slip at lower strains to slip on two slip systems at larger strains. As the crystal lattice rotates and stresses build in the x and y directions, the crystals are able to accommodate the deformation more easily with multiple active systems. Due to the angle of the slip plane, slip constraints at the boundaries are not as severe for the second slip system, so the strain hardening rate is reduced.

3.1.5 Mesh Refinement

The effect of mesh resolution on the solution is investigated by rerunning the 5-μm-thick simulation using twice as many elements in each direction. The results from the 40x200 mesh are shown along side of the 20x100 mesh results in figure 5. Other than the expected differences in smoothness of the fields, the nonlocal stress and slip rate distributions do not appear to be influenced significantly by halving the mesh size.

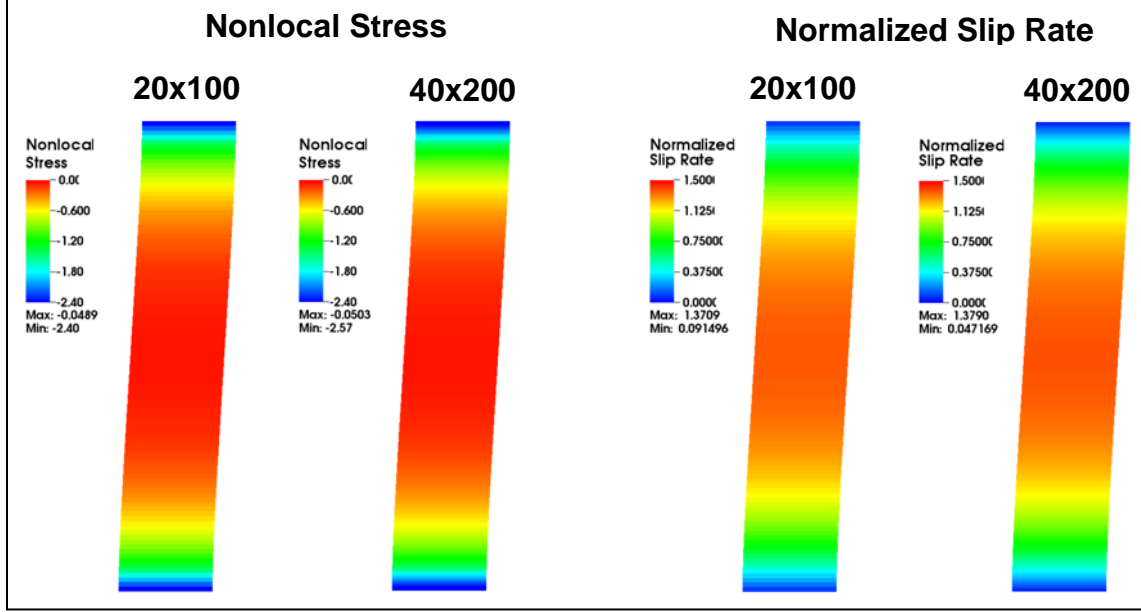


Figure 5. Comparison of nonlocal stress and the slip rate for the 20x100 and 40x200 element simulations of the 5- μm -thick single crystal. The results are shown at a 0.05 shear strain.

For a more quantitative assessment, the applied shear stress computed at the crystal boundaries is 2.3% lower for the finer mesh. Part of the difference may be due to the lower energy solution expected with an increased number of degrees of freedom, and the remainder can be attributed to discretization error associated with the nonlocal computations and the operator split algorithm. The time step was also a factor of two lower in the fine mesh calculation due to the dependence of the Courant stable time step on the mesh size. The smaller time step improves the accuracy of the operator split integration.

3.1.6 Time Step Instability

The simulation of the 0.5- μm -thick crystal experienced numerical instabilities when the strain increment per step was too great. This is thought to be associated with the operator split where the strength increase from the slip gradients creates a driving force that is too large and over-corrects the slip rate. Specifically, with a strain increment of 1.54×10^{-7} per time step, the slip rate for the 0.5- μm crystal was erratic and non-zero only in scattered, isolated elements. These isolated regions of slip occurred briefly and died out quickly as deformation proceeds, and eventually strain was incremented in the entire domain, albeit unevenly. When the time step was reduced by a factor of two, such that the strain increment per step was 7.43×10^{-8} , the calculation was well behaved. The results in figures 2 through 4 were run with a strain increment of 3.853×10^{-8} to be certain that the time step was small enough to suppress the instability. The calculations for the larger crystal sizes experienced less gradient hardening, and they were run at the Courant stable time step without any additional time step controls.

3.2 Polycrystal

An idealized polycrystal was created by filling a rectangular region with regular hexagonal grains (figure 6a). Simple shear boundary conditions were applied by prescribing velocities to the nodes on the upper and lower surfaces. Periodic boundary conditions were applied on the left and right surfaces. The orientation of the triangular crystal lattice in each of the grains was random, and the rotation angle from the reference orientation is indicated on the plot. The half grains at the same height on the left and right of the model region were given the same orientation to facilitate application of periodic boundary conditions. As with the single crystal simulations, the initial velocity of all interior nodes was prescribed to eliminate ringing from abrupt imposition of boundary conditions.

The default inter-element slip rate condition for all elements is that any element face touching another grain will have restricted slip. This is imposed by assuming that a ghost element across the interface has equal and opposite slip in equation 8. The restricted slip condition is enforced on the upper and lower surfaces and on grain boundaries, including those grain boundaries on the periodic surfaces. The half crystals on the periodic surfaces are treated differently; the element across the interfaces is assumed to have the same slip. This is not a truly periodic condition, but a data structure identifying periodic neighboring elements is not yet available.

Three model sizes are investigated: $160\sqrt{3} \mu\text{m} \times 300 \mu\text{m}$, $16\sqrt{3} \mu\text{m} \times 30 \mu\text{m}$, and $1.6\sqrt{3} \mu\text{m} \times 3 \mu\text{m}$. All use the same mesh configuration, scaled to give the appropriate dimensions. Each of the 88 hexagons was discretized by an identical mesh of 2112 quadrilateral elements (figure 6b). Nodes are shared along the grain boundaries, so the deformation is continuous throughout.

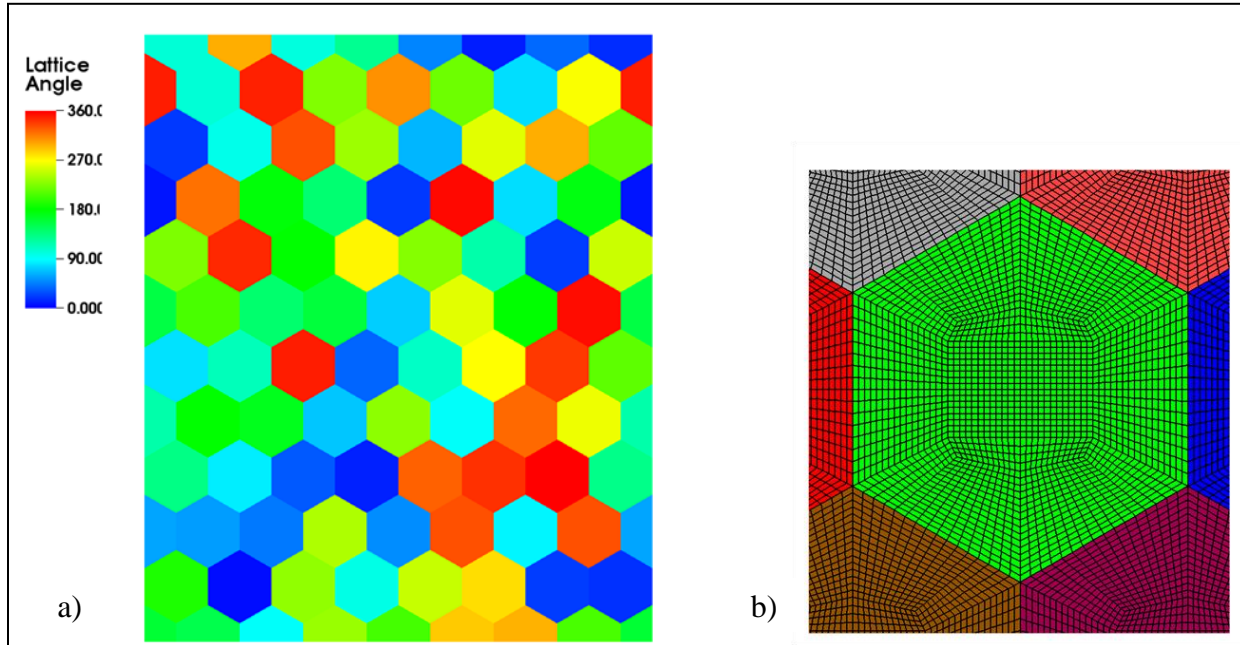


Figure 6. Grain structure (a) and finite element mesh and (b) for the polycrystal simulations.

3.2.1 Slip Rate

Slip rates normalized by the applied shear rate are shown in figure 7 for the three polycrystal sizes. At the larger crystal size, the strain rate localizes into well-defined bands. The majority of the deformation is carried by two horizontal bands with some scattered activity in the central region of the model. Blocks of grains appear to remain elastic while localized shear along the horizontal and vertical bands accommodates the deformation between neighboring blocks. The bands do not follow the grain boundaries, but many are associated with grain boundary triple points.

At the intermediate polycrystal size, the nonlocal slip constraint diffuses the deformation. The slip bands are still fairly well defined, but the peak strain rates are not as high and regions of nearly elastic behavior are smaller and less well defined. The slip rates in the 3.3- μm -thick polycrystal are considerably more diffuse and the material near the highly constrained top and bottom boundaries has the lowest strain rates. Grain outlines are evident as the slip rate tends to be high or low at the grain boundaries, and the color contrast across the boundaries accentuates them.

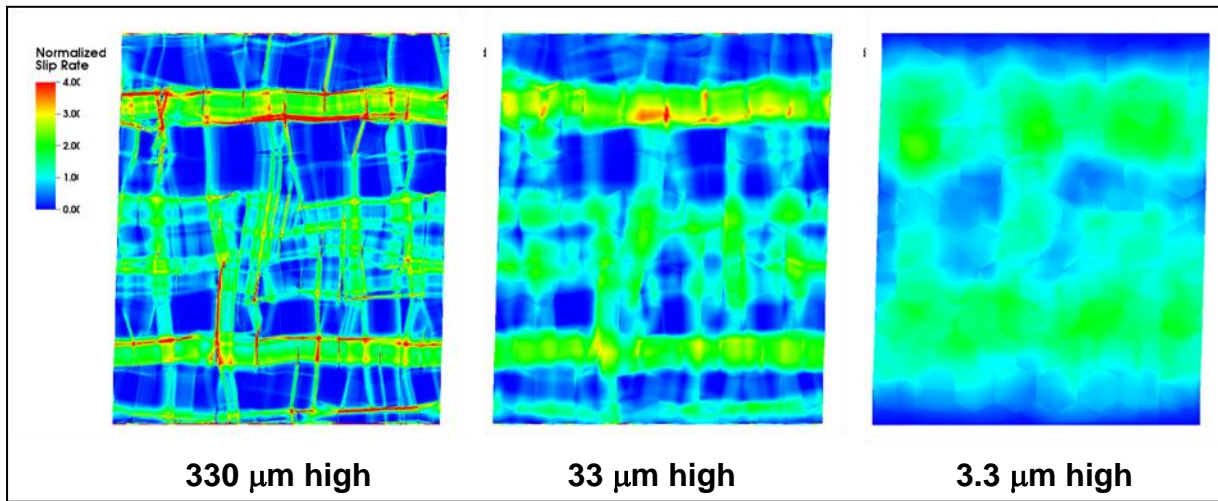


Figure 7. Normalized slip rate distribution for simple shear deformation of idealized polycrystals with heights of 330, 33, and 3.0 μm . The color scale is the same for all three plots.

3.2.2 Nonlocal Strengthening

The nonlocal strengthening associated with the gradients is shown in figure 8 for all three slip systems and the three crystal sizes. The color scale in each row is the same so that the magnitude of the effect of the slip systems can be compared. The scales are different for each crystal size as the strengthening is much greater in the smaller model region. The color scale on for the 330-mm polycrystal is set to a relatively low value of 0.5 MPa, and even then, the gradient contribution is only evident at the grain boundaries or near the most highly shear regions shown in figure 7. The impact on the solution is minor.

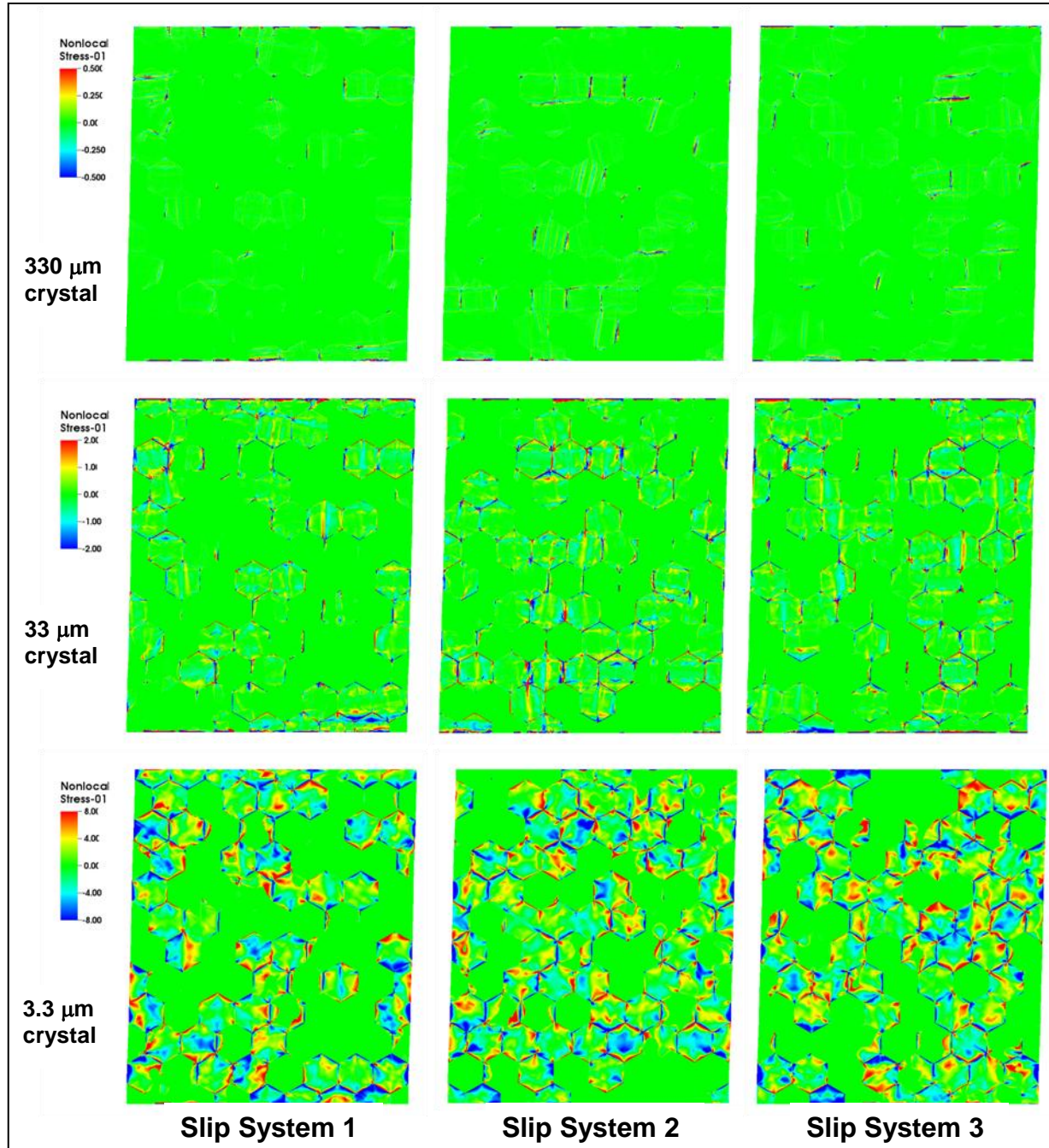


Figure 8. Nonlocal strength contributions on the three slip systems for polycrystal model sizes of 330, 33, and 3.3 μm . The color scales are consistent within each row.

The nonlocal strength distribution in the 33- μm polycrystal appears in the grain interiors as well as at grain boundaries. The strong interior features are associated with stress concentrations at grain boundary triple points, and most correspond to elevated slip activity in figure 7. Many of the grain boundaries show strengthening on one side and softening on the other. These

correspond to increasing slip when approaching grain boundaries for strengthening and decreasing slip when approaching the boundaries for softening.

The nonlocal strengthening is quite prominent in the 3.3- μm polycrystal. As with the intermediate size polycrystal, the sign of the gradient effect is often flipped across the grain boundaries. For most grains, the gradient is strongest at the grain boundaries and decays toward the grain center. However, there are a few notable grains where the peak values are in the interiors. These correspond to locations of intersecting slip activity in figure 7. The hyperbolic tangent function causes the gradient effect to saturate at a level between 12 and 13 MPa. It is also notable that the gradient strengthening occurs on only two of the three slip systems. This reflects the lack of redundant slip for the idealized crystal. Only two slip systems are active at any time.

3.2.3 Polycrystal Stress-strain Behavior

The shear stress-shear strain response for the three polycrystal sizes is presented in figure 9. As with the single crystals, the stress is higher for the smaller polycrystals. The nonlinearity with length scale is also clearly evident. There are, however, two important distinctions from the single crystal results. The first is that the initial yield point varies with crystal size, whereas it did not for the single crystal simulations. This is thought to be related to the single crystals yielding throughout simultaneously, while the polycrystal yields gradually and may build up local slip gradients before the macroscopic yield is evident.

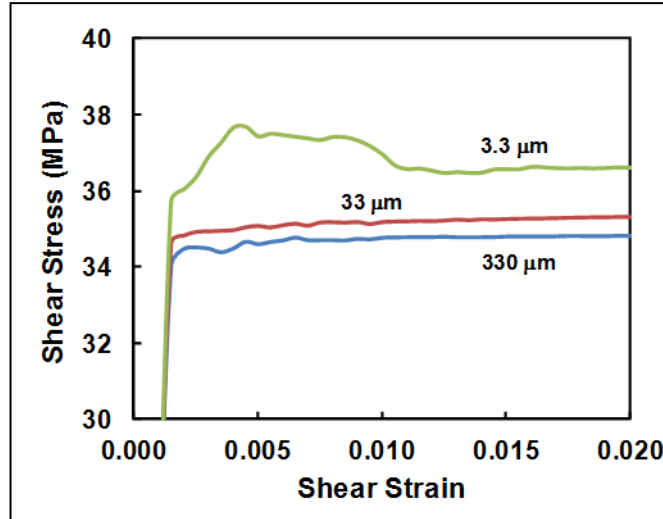


Figure 9. Shear stress strain response for three different size scales of idealized polycrystals.

The other notable difference is that the curves are not smooth. This could result from a combination of the evolution of the crystal lattice orientation, evolution of the slip gradients, and wave propagation in the explicit dynamic calculation. The change in lattice orientation is shown in figure 10 for the largest and smallest size scales. In the 330- μm polycrystal, where the strain localization is more pronounced, lattice reorientation is also localized. The local geometric

softening facilitates the shear. In contrast, due to the slip continuity and gradient constraints, the lattice reorientation in the 3.3- μm polycrystal is smoothed over a larger region relative to the grain size, and the lattice within the grains rotates nearly uniformly. A larger portion of the polycrystal had to realign, which takes longer and results in a greater load excursion before it settles into a nearly steady shear mode.

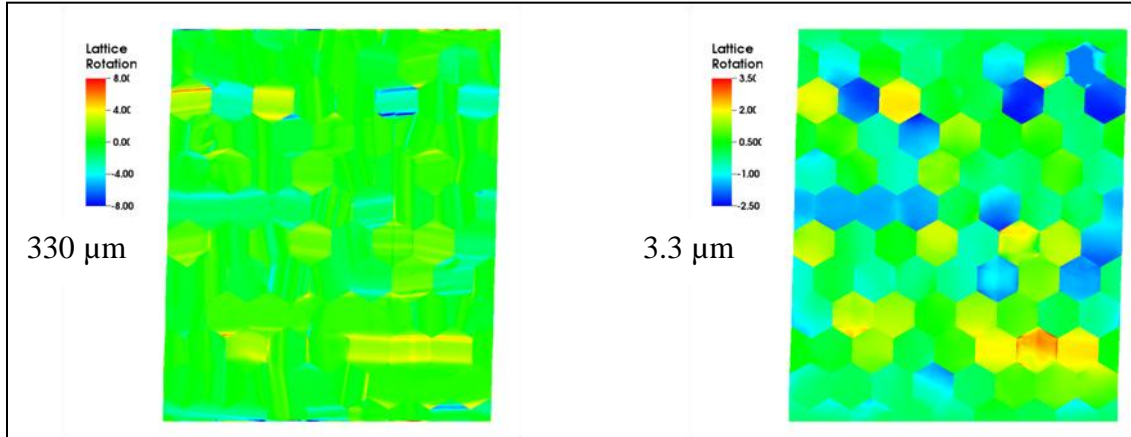


Figure 10. Change in crystal lattice orientation, in degrees, at 0.025 shear strain for the 330- and 3.3- μm high polycrystals.

4. Considerations for Discreteness of Dislocations

The motivation for imposing dislocation flux constraints is that dislocations are discrete entities that propagate from one element to the next as part of the slip process. Another aspect of the dislocation discreteness is their spacing, which is typically quantified in terms of the dislocation density. For well-annealed metals, a typical dislocation density is $10^6 - 10^7 \text{ cm}^{-2}$; at a few percent deformation, this increases to $10^8 - 10^9 \text{ cm}^{-2}$; and for a very heavily deformed polycrystal, the dislocation density is in the neighborhood of 10^{11} cm^{-2} (Hull and Bacon 1984). Table 1 lists the element areas for each of the four simulations in section 3.1 and the higher values of dislocation density for well-annealed, lightly deformed, and heavily deformed polycrystalline metals. From these values, an average number of dislocations enclosed by an element is calculated.

Table 1. Average number of dislocations per element expected in the simulations of section 3.1 for well-annealed, lightly deformed, and heavily deformed metals.

	50 μm Crystal $E_{\text{length}} = 0.5 \mu\text{m}$ $E_{\text{area}} = 0.25 \mu\text{m}^2$	5 μm Crystal $E_{\text{length}} = 0.05 \mu\text{m}$ $E_{\text{area}} = 0.0025 \mu\text{m}^2$	1 μm Crystal $E_{\text{length}} = 0.01 \mu\text{m}$ $E_{\text{area}} = 0.0001 \mu\text{m}^2$	0.5 μm Crystal $E_{\text{length}} = 0.005 \mu\text{m}$ $E_{\text{area}} = 0.000025 \mu\text{m}^2$
$10^7 \text{ cm}^{-2} (10^{-1} \mu\text{m}^{-2})$	1/40	1/4000	10^{-5}	2.5×10^{-6}
$10^9 \text{ cm}^{-2} (10^1 \mu\text{m}^{-2})$	2.5	1/40	1/1000	1/4000
$10^{11} \text{ cm}^{-2} (10^3 \mu\text{m}^{-2})$	250	2.5	1/10	1/40

The entries in table 1 that are less than 1.0 indicate that not every element will contain a dislocation. For example, 1/4000 means that one out of every 4000 elements can be expected to contain a dislocation. An implicit assumption in continuum crystal plasticity models is that the dislocation content in the elements is sufficient for slip to be smooth and continuous. It is clear that these conditions are not met for a well-annealed metal using any of the meshes in section 3.1, since not every element would contain even one dislocation. Using the discretization provided by the 50- μm -thick crystal simulation, a sufficient number of dislocations would be represented within each element when the crystal is heavily deformed, but not in the deformation leading up to that state. Considering that dislocations are usually not uniformly distributed, element sizes of a few microns may be necessary to assure a sufficient number of dislocations per element for a proper continuum crystal model representation.

Several aspects of crystal deformation cannot be represented accurately by a continuum model if elements are sparsely populated by dislocations. One difficulty is that only elements containing dislocations can slip, and other elements must either deform elastically or nucleate additional dislocations. A second feature not well represented is the discreteness of slip. A dislocation that passes through an element creates a slip increment $\Delta\gamma = b/E_{\text{length}}$. For a Burgers vector length of $b = 0.3 \times 10^{-3} \mu\text{m}$ and an element size of $E_{\text{length}} = 0.5 \mu\text{m}$, the slip must occur in increments of 0.6×10^{-3} rather than in the arbitrarily small increments permitted by the continuum representation. The discrete strain increment as a dislocation moves from one element to the next causes a commensurate increment in stress. This stress jump can be comparable to the yield strength. A final aspect of crystal plasticity, which cannot be represented properly if the element size is less than the dislocation spacing, is dislocation interactions leading to strengthening. Hardening and gradient effects are a result of interactions among dislocations. If the dislocations are sparse in the mesh, these interactions must be accounted for explicitly rather than implicitly in a hardening function.

4.1 Semi-discrete Dislocation Model

In an attempt to push continuum finite element simulations to smaller length scales where dislocations are sparse within the elements, a semi-discrete model was developed. It is run within a standard explicit-dynamic finite element framework that is described in Becker (2011). The

single slip constitutive model follows the traditional formulation with three major modifications: (1) only elements that contain dislocations or dislocation sources can slip; (2) the slip increment is quantized in terms of the Burgers vector and element size; and (3) elements designated to contain dislocation nucleation sources have a reduced flow strength. In addition to these slip model modifications, the code tracks dislocations moving from one element to another, and it also tracks the total number of dislocations that have traversed each element.

The quantization of the slip increment is created by starting with the standard continuum slip increment, $\Delta\gamma_{continuum}$, and using it to create an integer representing the number of Burgers vector lengths the dislocation traversed during increment.

$$N_{Burg} = \text{int} \left[\Delta\gamma_{continuum} \left(\frac{E_{length}}{b} \right)^2 \right] \quad (12)$$

The square of the dimensionless size scale loosely accounts for the step-by-step dislocation progression across the element. The slip increment used in the stress update is then calculated by

$$\Delta\gamma_{update} = N_{Burg} \left(\frac{b}{E_{length}} \right)^2 \quad (13)$$

Similar integer arithmetic is used to determine when a dislocation has completely traversed an element and will be transferred to a neighbor.

The crystal is assumed to generate dislocations dipoles at fixed nucleation sites. These dislocation nucleation sites are assigned randomly at the start of the simulation to a small fraction of the elements using a random number generator. The yield strength in these elements is also set to vary randomly between 25% and 75% of the yield stress. If the resolved shear stress in these elements exceeds the local yield strength, the crystal slips by moving dislocations from a dipole in opposite directions along the slip plane. Eventually these dislocations move to the neighboring elements. At this time the dislocations are transferred to the neighboring elements, and a new dislocation dipole initiates at the nucleation site. Elements with dislocations, but not nucleation sites, slip when the resolved shear stress exceeds the full 50-MPa yield strength. Elements without dislocations deform elastically.

The semi-discrete dislocation model is assessed through simulations using square elements with sizes 1.25, 0.125, and 0.025 μm . The element size is important as it is anticipated that the solutions will be mesh-size dependent. Calculations are run for different crystal sizes and several nucleation densities. In all instances, the simulations are simple shear with the single slip system orthogonal to the direction of shear. Periodic boundary conditions are applied as they were in section 3.1, and dislocation transmission is prohibited on the upper and lower surfaces where the shear is applied. The yield strength is 50 MPa, the shear modulus 30 GPa, the bulk modulus 60 GPa, and the Burgers vector $0.25 \times 10^{-3} \mu\text{m}$.

4.2 Semi-discrete Simulation Results

4.2.1 Low Density of Nucleation Sites

Simple shear simulations of well-annealed crystals with a low density of dislocation nuclei were run for model regions 50 μm wide and three model heights. The mesh was 400 elements wide. The region heights were 5, 10, and 100 μm , and the numbers of elements in the thickness direction were, respectively, 40, 80, and 800. This gives an element size of 0.125 μm in both x and y directions for all three models. The number of dislocation nucleation sites corresponding to these meshes is 7, 14, and 158, respectively. This provides roughly the same number of dislocations nucleation sites per unit area with a site density of approximately $3.2 \times 10^6 \text{ cm}^{-2}$. This is in the range of the dislocation density for a well-annealed metal.

The number of dislocations that passed through the elements at a shear strain of 0.01 is presented in figure 11. The complete simulation regions are shown for the 5- and 10- μm -high models. Only the top and bottom 10 μm of the 100- μm model are shown, since most of the center section appears as lines connecting the upper and lower portions. The most obvious feature is the discrete deformation. Slip occurs only along slip systems containing the nucleation sites. The slip traverses the crystal vertically along lines of elements that contains the slip planes. The remaining elements are elastic. Each of the 7 nucleation sites produced slip in the 5- μm crystal, and 13 of the 14 nucleation sites in the 10- μm model are evident. One of the nucleation sites in this crystal is near the bottom boundary and also near another nucleation site, and it does not slip. The 100- μm crystal contains more nucleation sites and many active slip planes are evident.

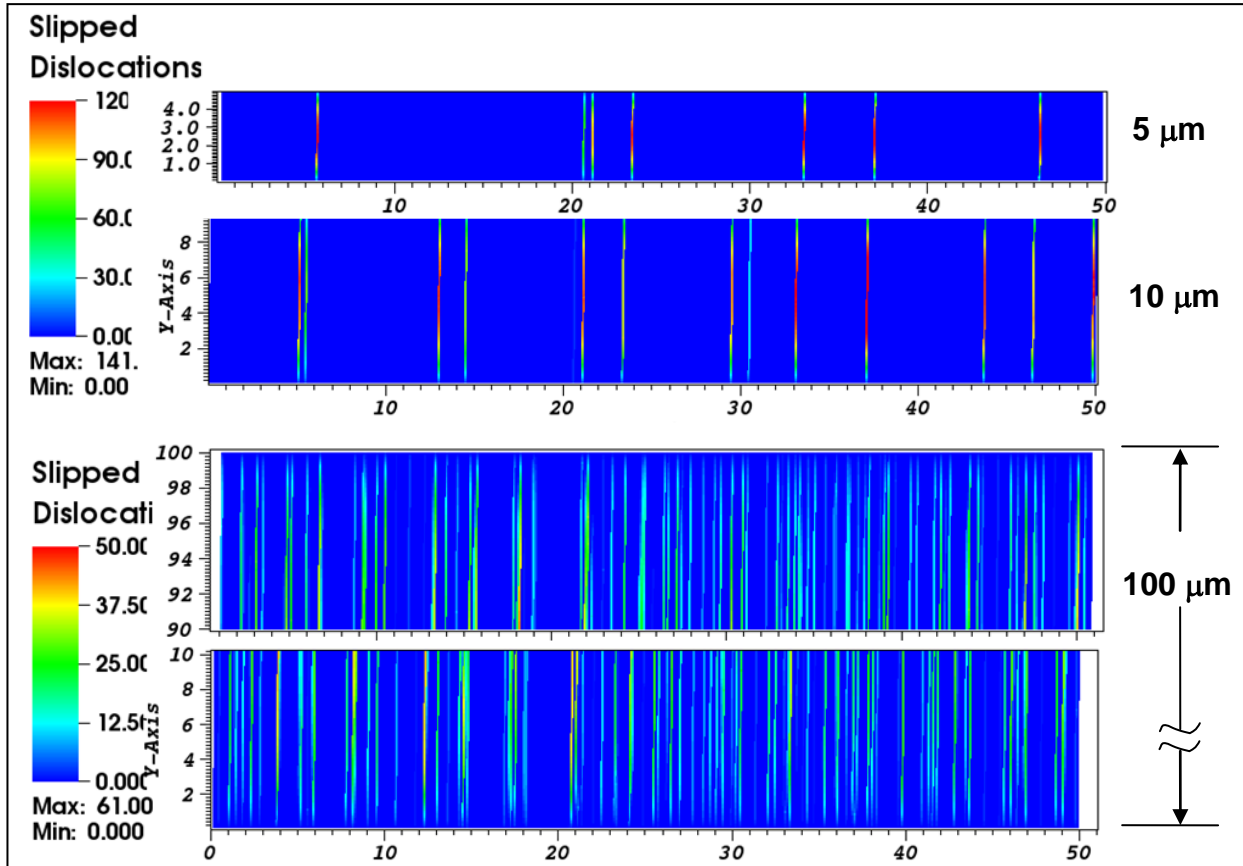


Figure 11. Number of dislocations passing through each element for the discrete dislocation simulations of three single crystal sizes indicated. The color levels for the 5- and 10- μm crystals are the same. The center 80 μm is omitted from the 100- μm crystal to highlight the gradients at the top and bottom surfaces.

An important feature of figure 11 is the slip gradient. Since dislocations cannot pass through the upper and lower boundaries, the slip (number of dislocations passed) at these surfaces is zero. The greatest number of dislocations has passed near the center of the crystal. The slip distributions along the 13 active slip planes of the 10- μm crystal are plotted in figure 12. The average of the 13 curves is plotted as a heavy black line, and the individual slip results are shown as the thin gray lines. All of the curves have a parabolic appearance near the boundaries. Several have a flat profile across the center. These are associated with slip planes that have dislocation nucleation sites near the surface, and they are also near more highly slipped systems. One of the dislocations emitted from the dipoles travels only a short distance to the boundary, and the back stress due to the pile up reduces the driving force for further nucleation. The other dislocation travels much of the way across the crystal before it meets elevated shear resistance from the pile-up at the other side of the crystal. The long travel distance creates the flat center region of the curve. Also, the nucleation sites near the boundaries produce fewer dislocations.

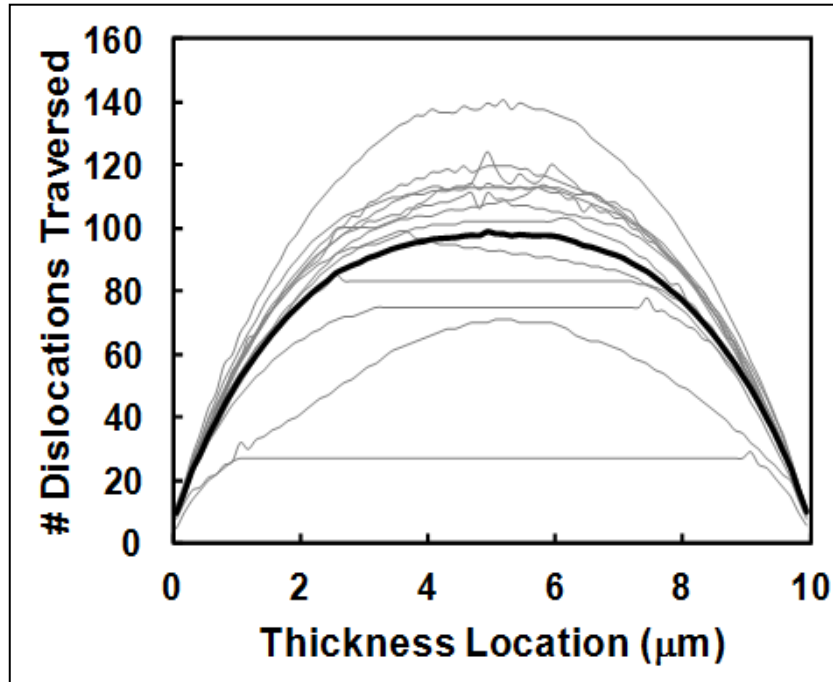


Figure 12. Number of dislocations passed through each element along the 13 active slip planes in figure 11 for the 10- μm -high crystal plotted against the through thickness location. The light lines are the individual results and the heavy, dark line is the average.

All of the dislocations must lie between the nucleation sites where they originate and the crystal boundaries. The slip distribution is directly related to the current positions of the dislocations. The dislocation positions are shown in figure 13. As with figure 11, the entire simulation regions are presented for the 5- and 10- μm -thick crystals, and only the upper and lower 10 μm are shown for the 100- μm thick crystal. Dislocations of opposite sign originating at the dipoles are shown by the red and blue. Dislocations of one sign move to the top and those of the other sign move to the bottom. The dislocation density is greatest at the boundaries and tapers off toward the center of the crystal. This is the classic picture of an edge dislocation pile-up. The dark red and blue elements on the crystal interior indicate the location of the dipole nucleation sites where dislocations can accumulate before gliding toward the boundaries.

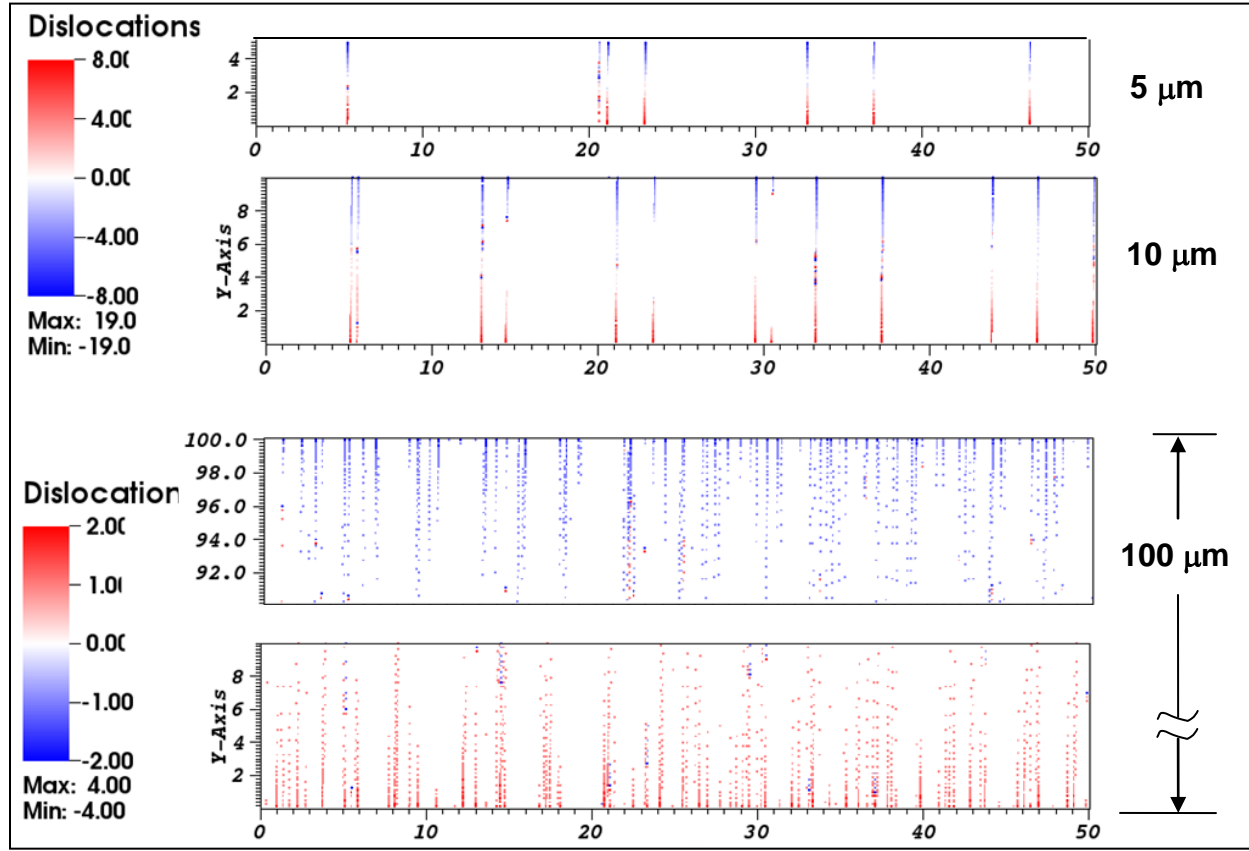


Figure 13. Number of dislocations currently within each element for the discrete dislocation simulations of three single crystal sizes. The color levels for the 5- and 10- μm crystals are the same. The center 80 μm is omitted from the 100- μm crystal to highlight the gradients at the top and bottom surfaces.

Each element can contain multiple dislocations, and the elements adjacent to the boundaries of the smaller two crystal sizes contain an average of 16. That average drops to seven in the next element away from the boundary, demonstrating a large gradient in dislocation density at the crystal boundaries. The first six elements along the slip planes and near the surface all contain dislocations in these two simulations. Most slip planes only have a few elements without dislocations along their entire lengths. Hence, the dislocation density is relatively dense for the 5- and 10- μm crystal heights.

The situation is different for the 100- μm -high crystal. With many more nucleation sites and dislocations to carry the deformation, the driving force and pile-ups are much less severe for the 100- μm crystal, and the maximum number of dislocations per element is four. Here the gradient is evident in the sparseness of elements containing dislocations. Near the surface most elements along the slip planes contain dislocations, but as the distance from the boundary increases, the elements containing dislocations become increasingly sparse.

The discrete slip creates a highly nonuniform stress field, which is illustrated by the in-plane stress components of the 10- μm -high crystal presented in figure 14. The shear stress, Sig-XY , is

low along the slip planes due to sliding, and it builds up between the slip planes. The slip planes effectively partition the domain into finite size elastic blocks, each undergoing simple shear with the shear stress on the lateral boundaries set by the slip resistance on the slip planes. The shear stress rises toward the interior of the blocks as the distance from the shear stress lateral boundary condition increases. Displacement is prescribed on the upper and lower boundaries. This imposes an additional constraint that keeps the boundary nodes uniformly spaced in the horizontal direction, and the shear stress is more or less uniform along the upper and lower surfaces.

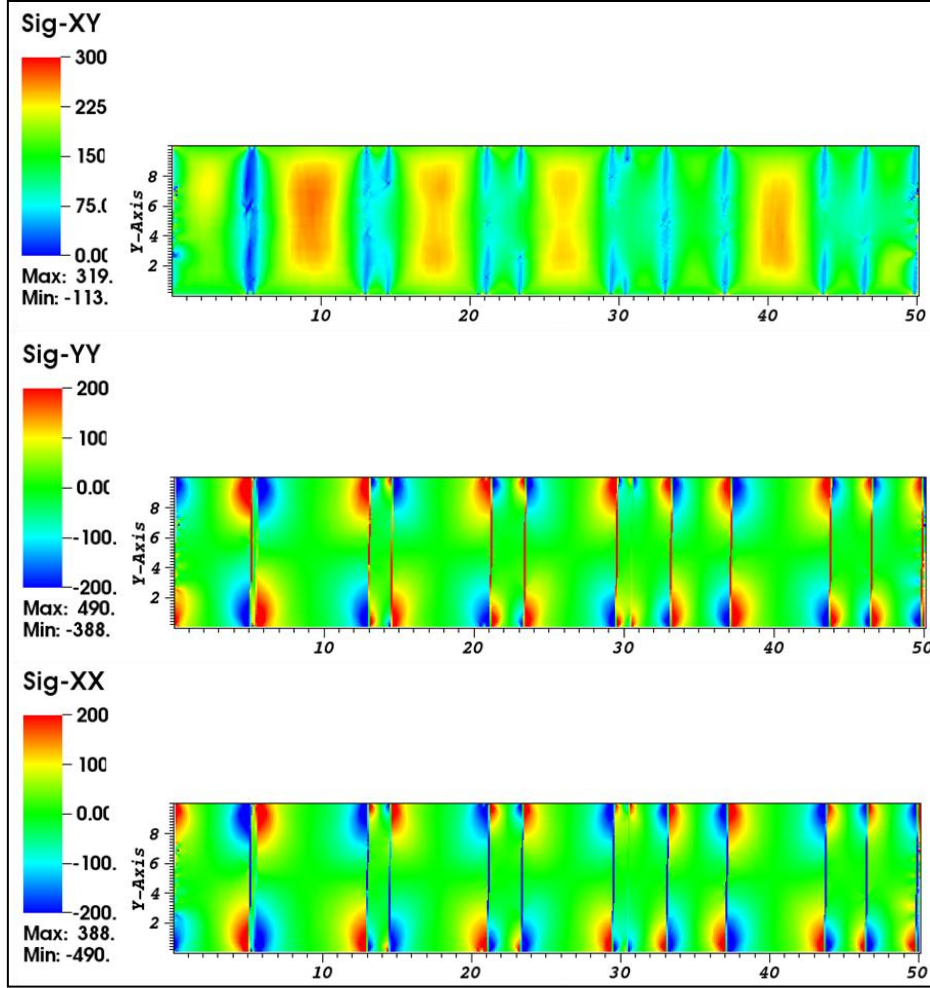


Figure 14. Plots of the in-plane stress components at a strain of 0.01 for the 10- μm -high single crystal deforming by discrete single slip on 13 slip planes.

As would be expected from an elastically sheared block, the corners experience significant normal stress, Sig-YY , as the blocks try to shear and rotate between the rigid platens. At every material point, the momentum equation in the vertical direction relates the gradient of Sig-YY in the vertical direction to the gradient of Sig-XY in the horizontal direction. The vertical Sig-YY gradient adjacent to the slip planes is small near the boundary and becomes approximately constant (linear stress profile) in the mid-thickness of the crystal. This coincides with the

horizontal shear stress gradient adjacent to the slip planes being small at the boundary and nearly constant in the mid-thickness region. Likewise, the horizontal gradient in the Sig-XX stress is related to the vertical gradient in Sig-XY , and similar gradient correlations can be made.

4.2.2 Moderate Density of Nucleation Sites

The simulations of section 4.2.1 were repeated with a tenfold increase in the number of dislocation nucleation sites. These were 92, 172, and 1600 for the 5-, 10-, and 100- μm -high single crystals. This gives a nucleation site density of approximately $3.2 \times 10^7 \text{ cm}^{-2}$.

Plots of the dislocation locations are shown in figure 15 for the 5- and 10- μm -thick single crystals deformed in simple shear to a strain of 0.01. As in the simulation with a low nucleation site density, the dislocation dipoles split with dislocations of one sign moving toward the upper surface and dislocations of the opposite sign move toward the bottom surface. However, since there are significantly more dislocations to accommodate the strain, they do not travel as far as in the prior analysis. The opposite signed dislocations are not as segregated and the total number of dislocations in the elements at the boundaries is significantly less. The results for the 100- μm simulation are not shown. This calculation had even more nucleation sites, less slip, and few dislocations accumulated at the boundaries. Consequently, segregation of the opposite-signed dislocations to the top and bottom surfaces was not apparent at a strain of 0.01.

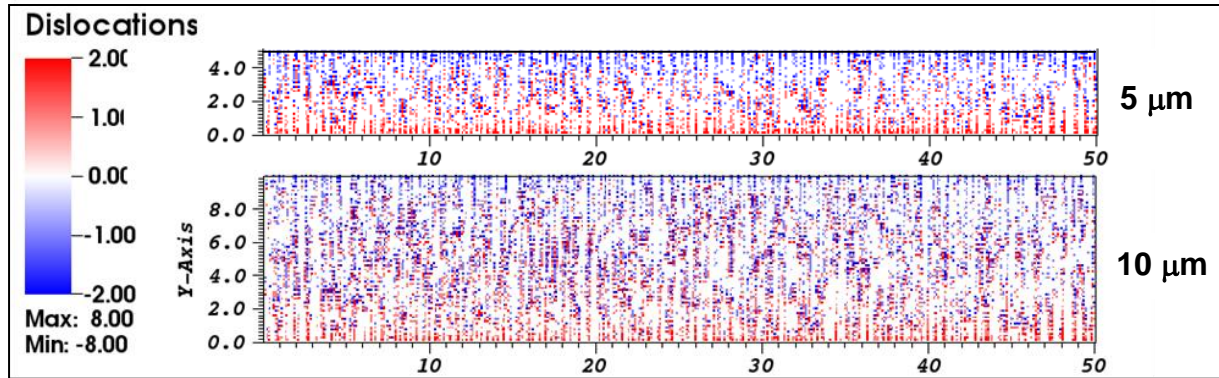


Figure 15. Number of dislocations within each element for discrete dislocation simulations of the 5- and 10- μm single crystals with a moderate density of nucleation sites.

The dislocations in these moderate source density calculations are much closer together than in the low nucleation source runs of section 4.2.1. As a result, the dislocations are too close for the finite element discretization to resolve the stress field satisfactorily (figure 16). So while the motion of the dislocations in figure 15 appears to be rational, the lack of sufficient spatial resolution to resolve the stress gradients renders the solution questionable. A larger element size would result in more elements containing dislocations, and the stress resolution would degrade further. Use of a smaller element size would allow more elements between dislocations to better resolve the field gradients.

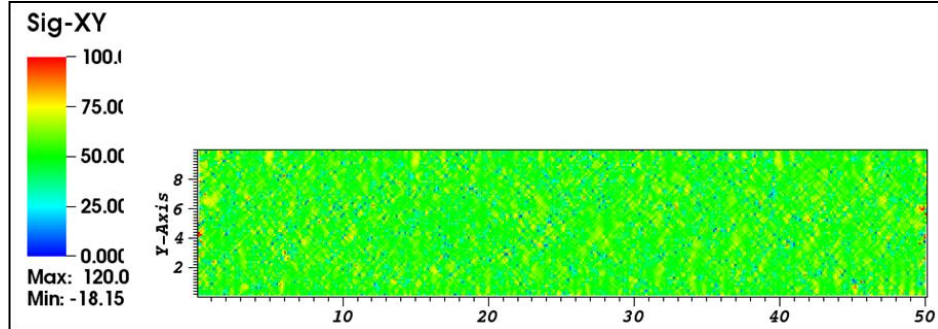


Figure 16. Shear stress distribution for 10- μm -thick crystal simulation with a moderate dislocation nucleation site density.

4.2.3 Reduced Element Size

Another set of simulations was run to explore the effect of element size. The mesh dimensions used in sections 4.2.1 and 4.2.2 were reduced by a factor of 5 in each direction such that the crystal width is 10 μm and the heights were 1, 2, and 20 μm . The element dimension for these simulations was 0.025 μm . The dislocation nucleation site seeding used in the mesh of section 4.2.2 was also used here, so the number of dislocation nucleation sites is the same as in section 4.2.2. However, the resulting nucleation site density is 25 times greater than in section 4.2.2 (approximately $8 \times 10^8 \text{ cm}^{-2}$ for each of the three crystal sizes) because the mesh is a factor of 5 smaller in each direction. An alternative configuration would have been to keep the nucleation site density constant, but with the higher spatial resolution, that would have resulted in fewer slip planes than are evident in figure 11.

The dislocation locations from these three simple shear runs are shown in figure 17 at a strain of 0.01. As with the previous simulations, the full crystal heights are shown for the smaller two crystal sizes and only the top and bottom 10% of the tallest crystal is shown. Also similar to the previous simulations, the dipole nucleation sites create oppositely signed pairs of dislocations that glide up and down toward the model boundaries. Pile-ups are evident, and it appears that the dislocations are more distinct and separated relative to the crystal height than those in figures 13 and 15. This is expected since the dislocation spacing is a physical distance and the model has effectively zoomed in by a factor of 5.

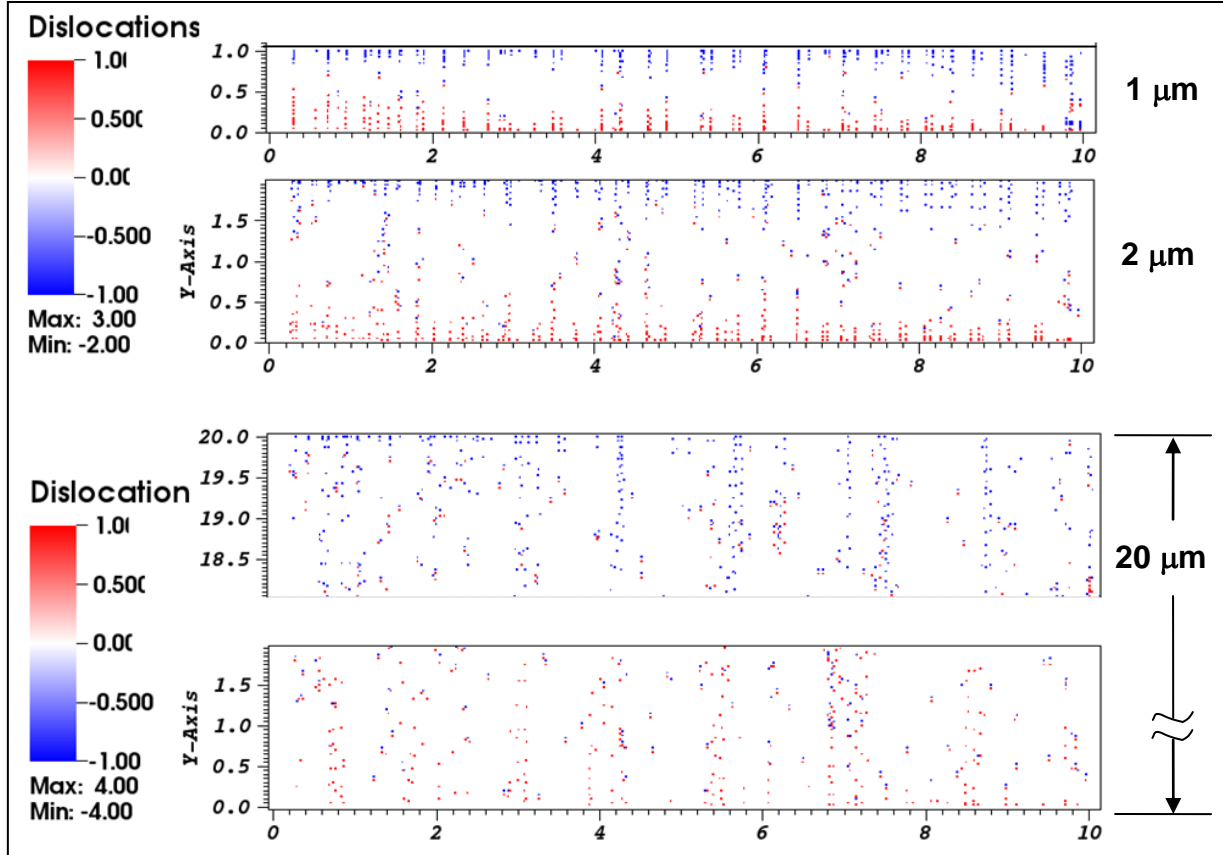


Figure 17. Number of dislocations currently within each element for the discrete dislocation simulations of three single crystal sizes. The color levels for the 1- and 2- μm crystals are the same. The center 16 μm is omitted from the 20- μm crystal to highlight the gradients at the top and bottom surfaces.

The slip planes in the 1- and 2- μm -high crystals appear distinct, and the dislocation pile-ups lie cleanly along the planes. In contrast, several of the nucleation sites in the 20- μm -high crystal have horizontal locations similar to other nucleation sites, resulting in closely spaced active slip planes. For these closely spaced slip planes, the locations of the dislocations near the surface appear to be coordinated. Such coordination could be related to a lower energy location in the interacting stress fields.

The shear stress field for this higher resolution simulation is shown in figure 18. As with the shear stress shown in figure 16, the spatial discretization is too coarse compared to the dislocation spacing to resolve the gradients. Many of the lowest stresses, indicated by blue in figure 18, are isolated. Consequently, the quality of the solutions is questionable.

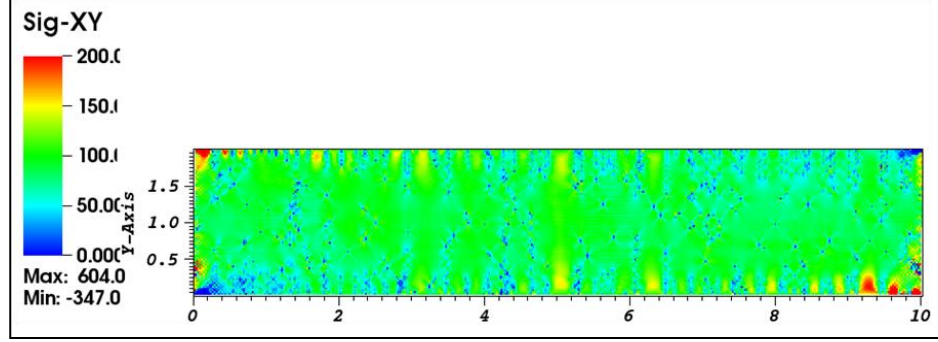


Figure 18. Shear stress distribution for the $10 \mu\text{m} \times 2 \mu\text{m}$ crystal in a calculation with an element size of $0.025 \mu\text{m}$ and 172 dislocation nucleation sites. The stress gradients are under-resolved.

An important piece of information on the shear stress plots is the minimum and maximum stress. In figure 16, the maximum is 120 MPa and the minimum is -18 MPa , whereas these are, respectively, 604 MPa and -307 MPa in figure 18. The reason can be traced to the quantized shear computed through equations 12 and 13. As a dislocation is about to leave an element, it exerts an elastic shear strain/stress on the neighboring element. As the dislocation crosses the element boundary and traverses the element, the shear stress through goes to zero and reverses sign. The stress due to the discrete shear peaks, and it has the opposite sign as the dislocation is leaving the element. Analytically, the shear stress is infinite at the dislocation core, and the spatial discretization effectively averages the stress over the element size. As the element size gets smaller, the peak stress represented in the mesh will increase, but the gradient is less well resolved. In figure 18, the peak shear stresses are an order of magnitude higher than the stress required for slip. Such high stresses dominate the solution and the error in the gradient overwhelms the slip resistance of the crystal. This is another reason that the quality of the solution is questionable.

4.2.4 Stress-strain Response from Semi-discrete Model

The shear stress-strain curves from the semi-discrete dislocation simulations are shown in figure 19. The element size, nucleation site density, crystal width, and crystal aspect ratio are indicated in the legends. The results from all of the simulations in section 4.2 are presented in addition to a set of three runs similar to those of section 4.2.2 but with the domains and elements 10 times larger. As discussed in earlier, the dislocations in this calculation are significantly under-resolved.

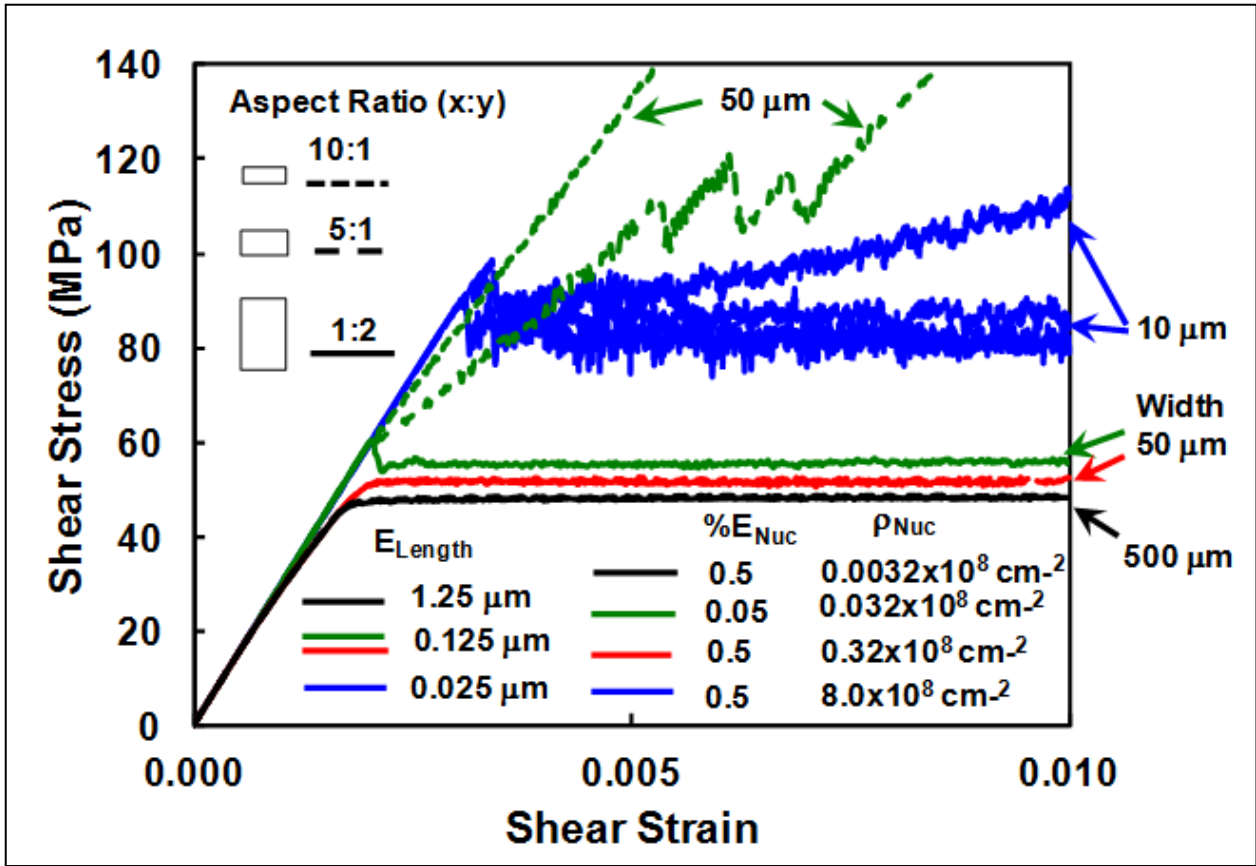


Figure 19. Shear stress-strain response for the semi-discrete crystal simulations of section 4. The legends and arrows show the model width, crystal aspect ratio, element length, and the percent of elements containing dislocation nucleation sites along with the corresponding nucleation site density. Curves of the same color have the same element size and element site nucleation percentage but different model aspect ratios.

The color groupings contain sets of three simulations where only the crystal height was varied. Within these sets of three curves of the same color, the results from the short crystals are represented by dotted lines, the intermediate height crystals are indicated by the dashed lines, and the tall crystals by the solid lines. In all cases, the stress increases as the crystal height decreases.

The green curves show the results from section 4.2.1 where the dislocation nucleation sites were sparse. The short crystal contained only seven active slip planes, and relatively large elastic regions are providing the shear stress resistance. The few slip planes do little to relieve the stress, and the result is nearly elastic. The intermediate height crystal was analyzed in some detail above. The additional slip planes created smaller elastic domains, and the stress relief provided by the slip planes is sufficient to have an appreciable impact on the overall stress. With the additional nucleation sites in the tall crystal, the elastic domains are small and the shear stress peaks and then saturates after a small drop.

The nucleation site density was increased by an order of magnitude over the green results to produce the red results, section 4.2.2. The mesh and model size are identical. Here there are sufficient dislocations to allow pervasive slip even for the shortest crystal. The stress saturates and is nearly the same for all three crystal heights. Using the same number of dislocation sites, the mesh size is then increased by a factor of 10 in both directions over the red curves to produce the black curves. Here too, the stress saturates and simulations for all three crystal heights give approximately the same shear stress. The shear stress is lower than the red curve because the singular shear stress near the dislocations is averaged over a large volume, and the resulting lower element stress near the dislocation lowers the overall shear stress. This simulation was not described in earlier sections.

The calculations producing the blue curves are described in section 4.2.3. This simulation had a mesh a factor of 5 smaller in each direction than the red curve, and the number of dislocation nucleation sites was the same. Even though there appears to be a sufficient number of dislocations in figure 17 to produce a smooth plastic response, the shear stress-strain curves are very noisy. The reason is the very high stress near the dislocations that results from the finer spatial discretization. Even though stress jumps occur over small volumes as the dislocations move from one element to another, the magnitude of the jump is sufficient to affect the average stress.

5. Discussion

The results from the continuum slip gradient model presented in section 3 demonstrate that an operator split approach can be used with an explicit dynamic time integration scheme to include gradient effects in crystal plasticity simulations. The nonlocal gradient formulation was an outgrowth of a penalty approach to enforce slip continuity between neighboring elements. The model was implemented into a large-scale parallel code with minimal disruption to the flow of the calculations. There appear to be additional time step restrictions for smaller element sizes, but the nature of the restrictions was not explored in the current investigation.

The single crystal and polycrystal results show the anticipated diffusion of sharp deformation fields and the expected stress-strain trends with size scale. While having the appearance of a successful modeling effort, a critical comparison of the model assumptions to the physical configuration, which it is supposed to represent, reveals a significant disconnect. This is particularly evident in the micron size range as the spatial resolution of the finite element grid is refined. An inherent assumption in the finite element crystal plasticity model is that microstructure features are either explicitly resolved by the grid or the microstructure is at a scale sufficiently smaller than the element size such that it can be approximated as a smoothly varying field. Similarly, a nonlocal gradient extension to the crystal model should resolve the gradient over several elements. As indicated above in table 1, the element size must be larger than $1 \mu\text{m}$

to have an average of one dislocation per element for a well-annealed material. At lower resolutions, the field within the element is not smooth and the discreteness of the microstructure is not resolved. A continuum crystal model at this or finer resolution does not provide a valid representation of the physical microstructure for an annealed crystal. Consequently, simulations cannot be expected to capture the microstructure mechanisms at this scale accurately.

Looking strictly at the dislocation density for heavily deformed metals, from table 1, it appears that the crystal model with submicron spatial resolution could represent a smeared dislocation microstructure within each element. However, dislocations are rarely uniformly distributed in heavily deformed metals. They typically organize into walls, which create a cell structure. The cell walls have a very high dislocation density, and the cell interiors have a low dislocation density. Extensive analysis of heavily deformed nickel by Hughes and Hansen (2000) shows that these cell sizes are greater than $0.1 \mu\text{m}$ after cold rolling to a 98% reduction, or a logarithmic strain in excess of 3.9. In order to have a smeared representation of such a cell microstructure within each element, the element size would have to be on the order of $1 \mu\text{m}$ or larger. Traditional crystal plasticity simulations using smaller element sizes will disregard a microstructure that could be resolved at that spatial resolution, and the computed deformation mechanisms may not be accurate.

As in the modeling of composites, refinement of the spatial discretization for the standard continuum crystal plasticity models has a limit when the element size begins to approach the length scale of important microstructure features. In order to have predictive microstructure-based simulations, the modeling strategy has to change with mesh refinement to match the physical microstructure at that refinement level. When the element size during mesh refinement of a composite approaches the size of the reinforcement, a homogenized continuum model is no longer appropriate, and the reinforcement and matrix phases should be modeled explicitly. There is nothing to prevent analysis using a homogenized model with elements smaller than the reinforcement, but the real mechanisms operating at that scale would be missed entirely. The calculations would not be predictive of mechanisms occurring at that resolution.

For pure metals, the limiting microstructure features for a crystal plasticity model are the dislocation spacing or the dislocation cell size, whichever is larger. These are typically on the order of 0.1 to $1.0 \mu\text{m}$. Further mesh refinement near this range of element sizes requires some explicit accounting for the dislocation microstructure and a change in the underlying constitutive relations. The continuum crystal model, including gradients, will run with smaller elements, but the solution will miss the effects of the discrete dislocation interactions and any mechanisms specific to dense dislocation walls and cell structures. It would give a false sense of a high resolution simulation since the microstructure governing the behavior is not captured spatially. The importance of accounting for the discreteness of dislocations in a pile up is highlighted by Roy et al. (2008) and Baskaran, et al. (2010). In general, however, mechanisms at this length scale have received little attention. Modeling at the size scale of precipitate or phase microstructure in alloys would also require further length scale considerations.

Nonlocal gradient calculations implicitly rely on the validity of the representation of the microstructure within the elements. If the element size is of the order of important microstructure features such that deformation mechanisms are not represented appropriately, the gradient calculations would not be based on reliable element data. Hence, gradient calculations are restricted to the same lower resolution limits.

A semi-discrete model based on the standard crystal plasticity model was investigated as an expedient method of crudely accounting for the discrete nature of dislocations at finer spatial resolutions. Only elements containing dislocations could slip plastically, and dislocations produce a definite level of slip after passing through an element. While the results of this simple model showed dislocation pile-ups and other expected features, the specific approach was unsatisfactory. The overriding issue is the singular stress field from the dislocations dominating the solution as the mesh was refined to resolve the stress gradients. The stress field is driven by the quantization of slip, which provides a higher stress magnitude related to the better resolution of the singularity at finer spatial resolutions. There does not appear to be a range of element sizes that will both resolve the stress field and not suffer from the effects of the singularity. Perhaps other semi-discrete approaches could be successful; this one was not.

Discrete dislocation dynamics simulations (e.g., Kubin et al., 1992 and Arsenlis et al., 2007) explicitly account for dislocations and their interactions and provide one means for incorporating dislocation microstructure at finer spatial resolutions. Finite element methods have been coupled with the discrete dislocation simulations through several approaches (Van der Giessen and Needleman, 1995; Fivel et al., 1998; Yasin et al., 2001). These types of formulations may be employed at the finer spatial resolutions in multiscale modeling schemes. There could be a transition from traditional continuum crystal plasticity to such a representation when the spatial resolution is fine enough, as in Wallin et al. (2008).

An area that has seen little model development activity is deformation associated with dislocation cell walls. In addition to being sources and sinks of dislocations for the cells, dislocations may run within some cell walls, causing slip. These walls could be treated as entities in resolved calculations of dislocations cells where they would interact with models of the cell interior which would transmit dislocations across the cells. This approach may be more efficient than modeling every dislocation within the cell walls. This is an area for future research.

6. Conclusion

A nonlocal crystal model based on the second gradient of crystal slip was implemented in a large-scale parallel finite element code, and the results show the expected trends of decreasing the severity of gradients and increasing strength with decreasing physical size. Although the model appears successful on the surface, there are concerns over the adequacy of the traditional

crystal model to represent the microstructure at smaller size scales. Elements smaller than the dislocation spacing or the dislocation cell dimensions cannot capture features of the deformation at that size scale accurately. This prompted exploration of a semi-discrete crystal plasticity model. The semi-discrete model also showed realistic results in terms of dislocation pile-ups, but the stress solution at the dislocation singularity dominated the solution at smaller element sizes, rendering the solution noisy and very mesh dependent.

The size scale of the microstructure of a typical pure metal, in terms of dislocation spacing and size of dislocation cells, is on the order of 0.1 to 1.0 μm . If the element size from a simulation is small enough to be within this range, the microstructure features and mechanism should be modeled explicitly in order to capture the lower length scale behavior. Models particular to this size scale are needed.

7. References

- Acharya, A. A Model of Crystal Plasticity Based on the Theory of Continuously Distributed Dislocations. *J. Mech. Phys. Solids* **2001**, *49*, 761–784.
- Arsenlis, A.; Cai, W.; Tang, M.; Rhee, M.; Oppelstrup, T.; Hommes, G.; Pierce, T. G.; Bulatov, V. V. Enabling Strain Hardening Simulations with Dislocation Dynamics. *Modelling Simul. Mater. Sci. Eng.* **2007**, *15*, 553–595.
- Arsenlis, A.; Parks, D. M.; Becker, R.; Bulatov, V. On the Evolution of Crystallographic Dislocation Density in Homogeneously Deforming Crystals. *J. Mech. Phys. Solids* **2004**, *52*, 1213–1246.
- Asaro, R. J. Micromechanics of Crystals and Polycrystals. *Advances in Applied Mechanics* **1983**, *21*, 1–115.
- Baskaran, R.; Akarapu, S.; Mesarovic, S. D.; Zbib, H. M. Energies and Distributions of Dislocations in Stacked Pipe-ups. *Int. J. Solids, Struct.* **2010**, *47*, 1144–1153.
- Becker, R. Effects of Crystal Plasticity on Materials Loaded at High Pressures and Strain Rates, *Int. J. Plast.* **2004**, *20*, 1983–2006.
- Becker, R. *Dislocation Transport in Continuum Crystal Plasticity Simulations*; ARL-MR-0799; U.S. Army Research Laboratory: Aberdeen Proving Ground, MD, 2011.
- Bittencourt, E.; Needleman, A.; Gurtin, M. E.; Van der Giessen, E. A Comparison of Nonlocal Continuum and Discrete Dislocation Plasticity Predictions. *J. Mech. Phys. Solids* **2005**, *51*, 281–310.
- Fivel, M. C.; Robertson, C. F.; Canova, G. R.; Boulanger, L. Three-Dimensional Modeling of Indent-Induced Plastic Zone at a Mesoscale. *Acta Mater.* **1998**, *46*, 6183–6194.
- Flanagan, D. P.; Belytschko, T. A Uniform Strain Hexahedron and Quadrilateral with Orthogonal Hourglass Control. *Int. J. Num. Meth. Engr.* **1981**, *17*, 679–706.
- Fleck, N. A.; Hutchinson, J. W. Strain Gradient Plasticity. *Adv. Appl. Mech.* **1997**, *33*, 295–361.
- Fleck, N. A.; Muller, G. M.; Ashby, M. F.; Hutchinson, J. W. Strain gradient Plasticity: Theory and Experiment. *Acta Metall. Mater.* **1994**, *42*, 475–487.
- Gao, H.; Huang, Y.; Nix, W. D.; Hutchinson, J. W. Mechanism-Based Strain Gradient Plasticity-I. Theory. *J. Mech. Phys. Solids* **1999**, *47*, 1239–1263.

- Gerken, J. M.; Dawson, P. R. A Finite Element Formulation to Solve a Non-Local Constitutive Model with Stresses and Strains due to Slip Gradients. *Comp. Meth. Appl. Mech. Engr.* **2008**, *197*, 1343–1361.
- Gurtin, M. E.; Anand, L.; Lele, S. P. Gradient Single-Crystal Plasticity with Free Energy Dependent on Dislocation Densities. *J. Mech. Phys. Solids* **2007**, *55*, 1853–1878.
- Hirschberger, C. B.; Peerlings, R.H.J.; Brekelmans, W.A.M.; Geers, M.G.D. On the Role of Dislocation Conservation in Single-Slip Crystal Plasticity. *Modelling and Simul. Mater. Sci. Eng.* **2011**, *19*, 085002, 1–24.
- Hughes, D. A.; Hansen, N. Microstructure and Strength of Nickel at Large Strains. *Acta Mater.* **2000**, *48*, 2985–3004.
- Hull, D.; Bacon, D. J. *Introduction to Dislocations*; 3rd Edition, Pergamon Press, Elmsford, NY.
- Kubin, L. P.; Canova, G.; Condat, M.; Devincre, B.; Pontikis, V.; Brechet, Y. Dislocation Microstructures and Plastic Flow: A 3D Simulation. *Diffusion and Defect Data-Solid State Data B* **1992**, *23–24*, 455–472.
- Lee, T. C.; Robertson, I. M.; Birnbaum, H. K. Prediction of Slip Transfer Mechanisms Across Grain Boundaries. *Scripta Metall.* **1989**, *23*, 799–803.
- Mayeur, J. R.; McDowell, D. L.; Bammann, D. J. Dislocation-Based Micropolar Single Crystal Plasticity: Comparison of Multi- and Single Criterion Theories. *J. Mech. Phys. Solids* **2011**, *59*, 398–422.
- ALE3D: An Arbitrary Lagrange-Eulerian 2D and 3D Code System, V-4.16 (2012), A. L. Nichols, ed., Lawrence Livermore National Laboratory.
- Peirce, D.; Asaro, R. J.; Needleman, A. Material Rate Dependence and Localized Deformation in Crystalline Solids. *Acta Metall.* **1983**, *31*, 1951–1976.
- Roy, A.; Peerlings, R.H.J.; Geers, M.G.D.; Kasyanyuk, Y. Continuum Modeling of Dislocation Interactions: Why Discreteness Matters? *Mater. Sci. Eng. A* **2008**, *486*, 653–661.
- Saha, R.; Xue, Z.; Huang, Y.; Nix, W. D. Indentation of a Soft Metal Film on a Hard Substrate: Strain Gradient Hardening Effects. *J. Mech. Phys. Solids* **2001**, *49*, 1997–2014.
- Schouwenaars, R.; Seefeldt, M.; Van Houte, P. The Stress Field of an Array of Parallel Dislocation Pile-Ups: Implications for Grain Boundary Hardening and Excess Dislocation Distributions. *Acta Mater.* **2010**, *58*, 4344–4353.
- Stölken, J. S.; Evans, A. G. A Microbend Test Method for Measuring the Plasticity Length Scale. *Acta Mater.* **1998**, *46*, 5109–5115.

Van der Giessen, E.; Needleman, A. Discrete Dislocation Plasticity-A Simple Planar Model. *Modelling Simul. Mater. Sci. Eng.* **1995**, *3*, 689–735.

Wallin, M.; Curtin, W. A.; Ristinmaa, M.; Needleman, A. Multi-Scale Plasticity Modeling: Coupled Discrete Dislocation and Continuum Crystal Plasticity. *J. Mech. Phys. Solids* **2008**, *56*, 3167–3180.

Yasin, H.; Zbib, H. M.; Khaleel, M. A. Size and Boundary Effects in Discrete Dislocation Dynamics: Coupling with Continuum Finite Element. *Mater. Sci. Eng. A* **2001**, *309–310*, 294–299.

NO. OF COPIES	ORGANIZATION	NO. OF COPIES	ORGANIZATION
1 ELEC	ADMNSTR DEFNS TECHL INFO CTR ATTN DTIC OCP 8725 JOHN J KINGMAN RD STE 0944 FT BELVOIR VA 22060-6218	1 PDF	US ARMY RSRCH LAB ATTN RDRL WMP C C WILLIAMS ABERDEEN PROVING GROUND MD 21005
2 HCS	US ARMY RSRCH LAB ATTN RDRL CIH C J KNAP ATTN RDRL CIH C P CHUNG BLDG 310E ABERDEEN PROVING GROUND MD 21005	7 HCS	US ARMY RSRCH LAB ATTN RDRL WMP C J CLAYTON ATTN RDRL WMP C R BECKER (4 COPIES) ATTN RDRL WMP C S BILYK ATTN RDRL WMP C T W BJERKE BLDG 390 ABERDEEN PROVING GROUND MD 21005
1 HC	US ARMY RSRCH LAB ATTN RDRL WML B B RICE ABERDEEN PROVING GROUND MD 21005	1 HC	US ARMY RSRCH LAB ATTN RDRL WMP D R DONEY (1 ELEC)
1 PDF	US ARMY RSRCH LAB ATTN RDRL WMM B B LOVE BLDG 393 ABERDEEN PROVING GROUND MD 21005	1 PDF	ATTN RDRL WMP E P SWOBODA (1 HC) BLDG 393 ABERDEEN PROVING GROUND MD 21005
1 PDF	US ARMY RSRCH LAB ATTN RDRL WMM J BEATTY 4600 DEER CREEK LOOP ABERDEEN PROVING GROUND MD 21005	2 PDFS	US ARMY RSRCH LAB ATTN RDRL WM P J BAKER ATTN RDRL WMP S E SCHOENFELD BLDG 309 ABERDEEN PROVING GROUND MD 21005
1 PDF	US ARMY RSRCH LAB ATTN RDRL WMM R DOWDING ABERDEEN PROVING GROUND MD 21005	1 PDF	US ARMY RSRCH LAB ATTN RDRL WM B FORCH BLDG 4600 ABERDEEN PROVING GROUND MD 21005-5066
1 PDF	US ARMY RSRCH LAB ATTN RDRL WMP B C HOPPEL BLDG 390 ABERDEEN PROVING GROUND MD 21005	1 PDF	US ARMY RSRCH LAB ATTN RDRL WM J MCCUALEY BLDG 4600 ABERDEEN PROVING GROUND MD 21005-5069
1 PDF	US ARMY RSRCH LAB ATTN RDRL WMP B S SATAPATHY ABERDEEN PROVING GROUND MD 21005	1 PDF	US ARMY RSRCH LAB ATTN RDRL WMP C D DANDEKAR BLDG 390 ABERDEEN PROVING GROUND MD 21005-5069
1 PDF	US ARMY RSRCH LAB ATTN RDRL WMP C B LEAVY BLDG 393 ABERDEEN PROVING GROUND MD 21005		

NO. OF
COPIES ORGANIZATION

2 HCS US ARMY RSRCH LAB
1 PDF ATTN IMAL HRA
MAIL & RECORDS MGMT
ATTN RDRL CIO LL TECHL LIB
ATTN RDRL SER L A WICKENDEN
(1 PDF)
ADELPHI MD 20783-1197